Assessment of the Long-Term High-Spatial-Resolution Global LAnd Surface Satellite (GLASS) Surface Longwave Radiation Product Using Ground Measurements

Qi Zeng, Jie Cheng, *Senior Member, IEEE*, and Lixin Dong

***Abstract*—In this article, we comprehensively assessed the newly released long-term high-spatial-resolution Global LAnd Surface Satellite (GLASS) surface longwave (LW) radiation product using site measurements of LW fluxes. In total, three years of ground-measured LW fluxes (surface longwave upward radiation (LWUP), surface longwave downward radiation (LWDN), and surface longwave net radiation (LWNR) collected from 141 sites in six independent networks (AmeriFlux, AsiaFlux, BSRN, CEOP, HiWATER-MUSOEXE, and TIPEX-III) are used to evaluate the GLASS LW radiation product. These sites cover various land cover types, surface elevations, and climatic types. According to the evaluation results, the biases are –4.33, –3.77, and 0.70 W/m^2 and the RMSEs are 18.15, 26.94, and 26.70 W/m^2 for clear-sky LWUP, LWDN, and LWNR, respectively. The GLASS LW radiation product performs well in climate-change-sensitive areas such as poleward areas, semiarid areas, and the "third pole", namely, the Tibetan Plateau. The accuracy of the GLASS LW product is higher or comparable to that of available LW products and studies but has a high-spatial-resolution of 1 km and a time span of 19 years. In conclusion, the overall accuracy of the clear-sky GLASS LW radiation product can satisfy the requirements of the hydrological, meteorological, and agricultural research communities on a global scale. We will continue to improve the retrieval algorithms and update the products accordingly.**

***Index Terms*—Global LAnd Surface Satellite (GLASS), hybrid method, longwave downward (LWDN), longwave net radiation (LWNR), longwave upward (LWUP), surface longwave (LW) radiation, surface radiation budget (SRB).**

Manuscript received January 15, 2020; revised April 8, 2020; accepted April 30, 2020. Date of publication May 6, 2020; date of current version May 22, 2020. This work was supported in part by the National Natural Science Foundation of China under Grant 41331173, in part by the National Key Research and Development Program of China under Grant 2016YFA0600101, and in part by the Second Tibetan Plateau Scientific Expedition and Research Program (STEP) under Grant 2019QZKK0206. *(Corresponding author: Jie Cheng.)*

Qi Zeng and Jie Cheng are with the State Key Laboratory of Remote Sensing Science, Chinese Academy of Sciences, Jointly Sponsored by Beijing Normal University and the Institute of Remote Sensing and Digital Earth, Beijing 100875, China, and also with the Institute of Remote Sensing Science and Engineering, Faculty of Geographical Science, Beijing Normal University, Beijing 100875, China (e-mail: 976426265@qq.com; brucechan2003@126.com).

Lixin Dong is with the Key Laboratory of Radiometric Calibration and Validation for Environmental Satellites, Beijing 100081, China, and also with the National Satellites Meteorological Center, Beijing 100081, China (e-mail: dlx_6666@163.com).

Digital Object Identifier 10.1109/JSTARS.2020.2992472

I. Introduction

THE surface longwave (LW) radiation (4–100 μm) is one of the two components of the surface radiation budget (SRB), and it consists of the surface longwave upward radiation (LWUP), the surface longwave downward radiation (LWDN), and the surface longwave net radiation (LWNR) [1], [2]. The surface LW radiation is a significant diagnostic parameter for land surface, atmospheric, and ocean models, and it is the most important variable for investigating biogeochemical processes, greenhouse effects, and global climate changes [3]–[9].

LW radiation can be measured directly at ground sites. However, ground-based measurements are expensive, and the sites are limited in number and sparsely distributed around the globe [10]. Satellite remote sensing is the only available technology for acquiring high-spatial-resolution LW radiation products. Substantial efforts have been made to use remote sensing to estimate of surface LW product, and many algorithms have been proposed.

From the land surface temperature (LST) and the surface broadband emissivity (BBE), LWUP can be directly calculated. Many satellite LST products are available, such as the Moderate Resolution Imaging Spectrometer (MODIS) LST product [11], the Visible Infrared Imaging Radiometer Suite LST product [12], and the Spinning Enhanced Visible and Infrared Imager (SEVIRI) LST product [13]. For BBE, the Global LAnd Surface Satellite (GLASS) BBE product is available [14]–[16]. Also, we can calculate the BBE from available spectral emissivity products such as the MODIS and ASTER emissivity products via spectral conversion [17]. However, there are larger uncertainties in the current LST and spectral emissivity products [18], [19], which will inevitably propagate into the calculated LWUP. Hybrid methods estimate the LWUP using linear or nonlinear combinations of the top of atmosphere (TOA) radiances via radiative transfer simulations and statistical regression [20]. The hybrid methods for estimating LWUP and LWDN are well recognized by the community and are gaining popularity due to their acceptable accuracy and ease of implementation [21]–[24].

LWDN was initially estimated using a bulk formula from the ground-measured meteorological and cloud parameters at local and regional scales. Many bulk formulae have been developed since then [25]–[31]. The bulk formulae have been

widely used due to their simplicity, easily obtained inputs, and acceptable accuracy [32], [33]. However, most bulk formulae are site-specific because their coefficients are determined by the site-measured meteorological and cloud parameters. The coefficients must be adjusted or calibrated when applied to other regions or large scales [27]. Similar to the estimation of clear-sky LWUP, the hybrid method is widely used to accurately estimate clear-sky LWDN. Regarding cloudy-sky LWDN, Zhou and Cess [6] proposed a method that requires the surface self-emission, column water vapor (CWV), and cloud liquid water path (LWP) as inputs, which has been used to estimate cloudy-sky LWDN by CERES. Afterwards, Zhou *et al*. improved the algorithm [34] by considering the ice water path (IWP) to avoid large errors in LWDN for regions where the atmospheric conditions near the surface tend to be extremely cold and dry. The single-layer cloud model [35] and multilayer cloud model [36] are also used to estimate cloudy-sky LWDN.

LWNR can be calculated either by subtracting LWUP from LWDN [22], [37] or by developing a direct method. For example, Zhou *et al*. [38] and Guo and Cheng [39] establish the empirical relationships between the surface net shortwave radiation and LWNR and estimate LWNR from the surface net shortwave radiation.

In addition to the remote sensing approach, we can calculate LW radiation using radiative transfer models. For example, Zhang *et al*. [40] used the radiative transfer model of the NASA Goddard Institute for Space Studies (GISS) of GCM to calculate the surface radiative fluxes. The uncertainties of daily LWUP and LWDN are 10–20 and 10–15 W/m^2, respectively. Then, this method was applied to produce the SRB products. Three satellite SRB products are available: the International Satellite Cloud Climatology Project-Flux Data (ISCCP-FD) [40]–[42], which are calculated using the radiative transfer model of the NASA GISS model of GCMs; the Global Energy and Water Cycle Experiment-Surface Radiation Budget (GEWEX-SRB) [43], [44], which is obtained using the ISCCP dataset; and the Clouds and the Earth's Radiant Energy System-Gridded Radiative Fluxes and Clouds (CERES-FSW) [46], which was produced by adopting a bulk formula [46] and GCM models [47]. They share the common features of coarse spatial resolution (100–280 km) and low validation accuracy [10], [48]–[50].

High-spatial-resolution LW radiation products (down to 1 km) provide important diagnostic parameters for mesoscale land surface and atmosphere models, particularly over heterogeneous areas [51], [52]. Additionally, high-spatial-resolution LW radiation products can serve as medium-scale products for the validation of coarse resolution data, as LWUP varies on much finer spatial scales [53]. However, high-spatial-resolution LW radiation products have rarely been reported. Thus, we developed the framework for producing a long-term all-sky 1-km instantaneous LW radiation product from MODIS data (http://glass.umd.edu/Download.html). This product was named the GLASS LW radiation product. In the developed framework, the hybrid methods that were developed by Cheng *et al*. [54], [55] were used to retrieve clear-sky LWUP and LWDN; the MODIS LST [56] and the GLASS BBE product [14], [15] were used to calculated cloudy-sky LWUP; and the single-layer cloud model [57] and the MODIS cloud parameter product were used to retrieve cloud-sky LWDN [58].

The hybrid methods were validated using limited ground measurements during the stage of algorithm development, with biases and RMSEs of 0.06 and 21.01 W/m^2, respectively, for LWUP, and 0.57 and 24.29 W/m^2, respectively, for LWDN. Recently, Zhou *et al*. [59] reported that our hybrid method for LWDN has a bias of 4.81 W/m^2 and an RMSE of 17.18 W/m^2 when verified with ground measurements that were collected from 148 sites. However, the accuracy of the produced LW radiation product remains unknown. Thus, it is necessary to determine the accuracy and uncertainty of the produced LW radiation product, which can facilitate the full investigation of the product quality and optimization of the algorithms by the product developer and facilitate its use by the users.

This study presents a comprehensive evaluation and analysis of the produced LW radiation product using ground measurements that were collected from 141 sites in six independent flux networks, which cover various land covers, surface elevations, and climatic types. The ground measurement and satellite datasets, the GLASS LW radiation retrieval algorithms, and the corresponding product are introduced in Section II. The evaluation results of the GLASS LW radiation product and the main characteristics of the errors are presented in Section III. Possible causes of errors are discussed in Section IV. Section V concludes this article.

II. Data

A. Ground Measurements

It is highly important to evaluate high-level remote sensing products with the ground-measured "ground-truth" data. In the evaluation of the LW radiation product that is produced in this study, the ground measurements of 141 commonly used sites from six independent flux networks that cover various land cover types, climatic types, and surface elevations are used as representative evaluation data. These sites include ten sites from the Asian network of flux stations (AsiaFlux) [60]; 30 sites from the AmeriFlux network [60]; 31 sites from the Baseline Surface Radiation Network (BSRN), of which 20 are without LWUP measurements; 40 sites from the Coordinated Enhanced Observing Period (CEOP); 19 sites from the Multiscale Observation Experiment on Evapotranspiration over heterogeneous land surfaces in the middle reaches of the Heihe River Basin (HiWATER-MUSOEXE) [61], [62]; and 11 sites from the Third Tibetan Plateau Atmospheric Scientific Experiment (TIPEX-III) [63]. The site distribution is shown in Fig. 1. We tried to collect three years of measurements for each network, but only several months of observations were collected for HiWATER-MUSOEXE and TIPEX-III.

Among the 141 sites from six networks, only 121 sites have LWUP measurements. All sites have LWDN measurements. LWNR is obtained by subtracting LWUP from LWDN; hence, we only consider 121 sites. There are 137 sites in the land and only 4 sites in the ocean. Kipp & Zonen net radiometers (CNR1, CNR4, or CNR1-lite) are used to measure LWUP and LWDN in AmeriFlux, AsiaFlux, HiWATER-MUSOEXE, and

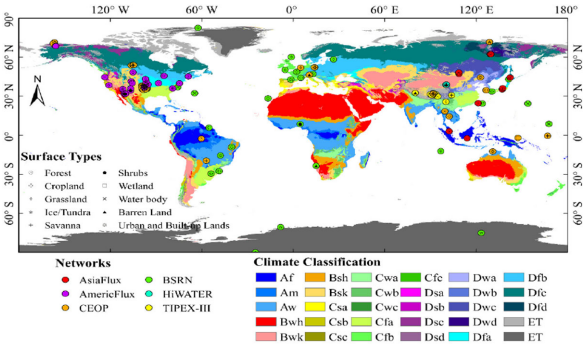

Fig. 1. Global distribution of validation sites from six flux networks and various climatic zones.

TIPEX-III. The spectral range of CNR1 is from 5.0 to 50 μm (https://www.campbellsci.com/cnr1), and the spectral range of CNR1-lite is 4.5–42 μm. LWUP and LWDN in BSRN and CEOP have been measured using Eppley precision infrared radiometers (PIRs) in the spectral response range from 3.5 to 50 μm and Kipp & Zonen CG 4 pyrgeometers in the spectral response range from 4.5 to 42 μm (http://www.kippzonen.com/?product/17152/CGR+4.aspx). In this study, the sites represent various land cover and climatic types. Their elevations vary from the sea level to 4730 m, and the site latitudes range from 89.98°S to 82.49°N. Table VII presents detailed information about the latitude, longitude, surface elevation, land cover type, climatic type, temporal resolution, considered time period, and measuring instruments for each site from the six observation networks.

B. GLASS LW Radiation Product

1) Clear-Sky LW Radiation Estimation Algorithms: From the perspective of radiative transfer theory, the basic principle for estimating clear-sky LWUP and LWDN is that the TOA radiances of the TIR channels contain information that is related to the surface temperature, emissivity, and LWDN [21], [22], [64]. The hybrid method establishes a linear or nonlinear relationship between clear-sky LWUP or LWDN and the TIR channel radiances via extensive radiative transfer simulations and statistical regression as

$$\mathrm{LWUP}_{\mathrm{clear}} = a_0 + a_1 L_{29} + a_2 L_{31} + a L_{32} \tag{1}$$

where L_{29}, L_{31}, and L_{32} are the TOA radiances for MODIS channels 29, 31, and 32, respectively, and a_0, a_1, a_2, and a_3 represent the regression coefficients. To incorporate the effects of the temperature difference between the surface and the atmosphere (the bottom layer temperature of the temperature profile), the global land surface was divided into three regions according to their latitudes: a low-latitude region (0°–30°N, 0°–30°S), a mid-latitude region (30°–60°N, 30°–60°S), and a high-latitude region (60°–90°N, 60°–90°S). First, we obtain the statistical range of the surface-atmosphere temperature difference using two years of data from the AIRS L2 product. Then, the range is used to guide the setting of the surface temperature in the radiative transfer modeling in the development of a hybrid method. Finally, we developed a hybrid method for each subregion. Additionally, to reduce effects of the thermal infrared directionality of the land surface, the angular bin strategy that was proposed by Liang *et al.* [65] was adopted. The coefficients of the hybrid method for view zenith angles of 0°, 15°, 30°, 45°, and 60° are developed. In total, 15 formulae are developed in our hybrid method [54].

In the developed hybrid method for estimating clear-sky LWDN, the strategy is similar to those of the bulk formula [33] and Zhou *et al.* [35]. LWUP is adopted as a proxy for the air temperature, the TOA radiance of MODIS channel 29 is used to characterize the water vapor in the lower atmosphere as its weighting function peaks at the surface, and CWV is also used as a predictor because it is the major greenhouse gas in the atmosphere and has the largest variation over a short time. The clear-sky LWDN is expressed as

$$\mathrm{LWDN}_{\mathrm{clear}} = a_0 + a_1 \mathrm{LWUP}_{\mathrm{clear}} + a_2 \log(1+\mathrm{CWV}) + a_3 \log(1+\mathrm{CWV})^2 + a_4 L_{29} \tag{2}$$

where CWV is the column water vapor. $\mathrm{LWUP}_{\mathrm{clear}}$ is LWUP computed via (1). We use a backup method to calculate clear-sky LWDN over a high-elevation area with extremely low CWV, which is expressed as

$$\mathrm{LWDN}_{\mathrm{clear}} = a \mathrm{CWV}^b \tag{3}$$

where a and b are the coefficients.

2) Cloudy-Sky LW Radiation Estimation Algorithms: The cloudy-sky LWUP is calculated from the surface temperature and the BBE as follows:

$$\mathrm{LWUP}_{\mathrm{cloudy}} = \sigma \varepsilon_s T_s^4 \tag{4}$$

where σ is the Stefan–Boltzmann constant; T_s is the surface temperature, which is extracted from MOD06/MYD06; and ε_s represents the surface broadband emissivity, which is obtained from the GLASS BBE product.

The cloud-sky LWDN is estimated from MODIS cloud parameters using the single-layer cloud model of Forman and Margulis [57], which is expressed as

$$\mathrm{LWDN}_{\mathrm{cloudy}} = \sigma \varepsilon_a T_a^4 + \sigma(1-\varepsilon_a)\varepsilon_c T_c^4 \tag{5}$$

where ε_a is the air emissivity, which is computed via the bulk formula that was proposed by Prata [31]; ε_c represents the cloud emissivity; and T_a and T_c are the air temperature at the screen level and the cloud-top temperature, respectively. ε_a is expressed as

$$\varepsilon_a = 1 - (1+\xi)\exp(-\sqrt{1.2+3\xi}) \tag{6}$$

$$\xi = \frac{46.5}{T_a} e_0 \tag{7}$$

$$e_0 = 6.11 \exp\left[\frac{L_v}{R_v}\frac{1}{273.15} - \frac{1}{T_d}\right] \tag{8}$$

where e_0 is the near-surface vapor pressure, which is computed from the dew temperature T_d [66]; L_v and R_v represent the latent heat of vaporization and the gas constant for water vapor, which are 2.5×10^6 kg^{-1} and 461 kg^{-1} k^{-1}, respectively; and T_a and T_d are both obtained from the surface temperature [58].

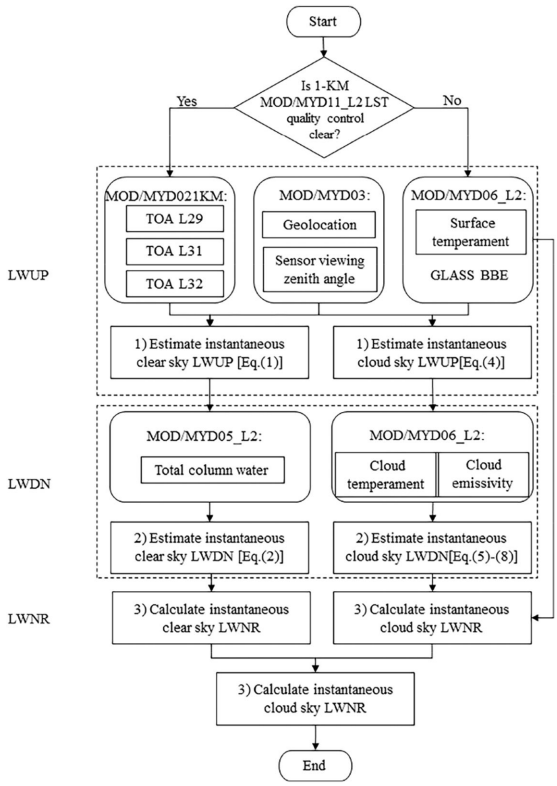

Fig. 2. Flowchart of the generation of GLASS LW radiation products.

3) Production of the GLASS LW Radiation Product: The production code for generating the GLASS LW radiation product was implemented in a high-performance computer [16]. The production process is illustrated in Fig. 2. The inputs include (1) the TIR TOA radiances of channels 29, 31, and 32 from the MOD021KM/MYD021KM product; (2) the CWV from the MODIS near-infrared channel atmospheric product (MOD05_L2/MYD05_L2); (3) cloud and surface parameters (the cloud sky surface temperature, cloud-top temperature, and emissivity) from MODIS cloud product MOD06/MYD06; (4) cloud mask flags from the MODIS cloud mask product (MOD35_L2/MYD35_L2) and the MODIS LST and emissivity product (MOD11_L2/MYD11_L2); (5) the geolocation and sensor viewing zenith angle from MODIS geolocation product MOD03/MYD03; and (6) the GLASS BBE product [15], [67]. Following the study of Cheng *et al.* [55], MOD11_L2/MYD11_L2 was used to identify clear-sky pixels over land, while MOD35_L2/MYD35_L2 was used to identify clear-sky pixels over ocean due to MOD11_L2/MYD11_L2 did not provide clear-sky LSTs over ocean. Another constraint is the latitude, which is used to select the clear-sky LWUP formulae for calculating LWUP. All-sky instantaneous (four times per day) 1-km LW radiation products are output in HDF format. The scientific datasets include geolocation, LWUP, LWDN, LWNR, and quality control datasets.

GLASS LW radiation products have been produced from two MODIS satellite observation platforms (Terra and Aqua), which span 19 years from 2000 to 2018 and are freely available to the public (http://glass.umd.edu/Download.html). Fig. 3 presents

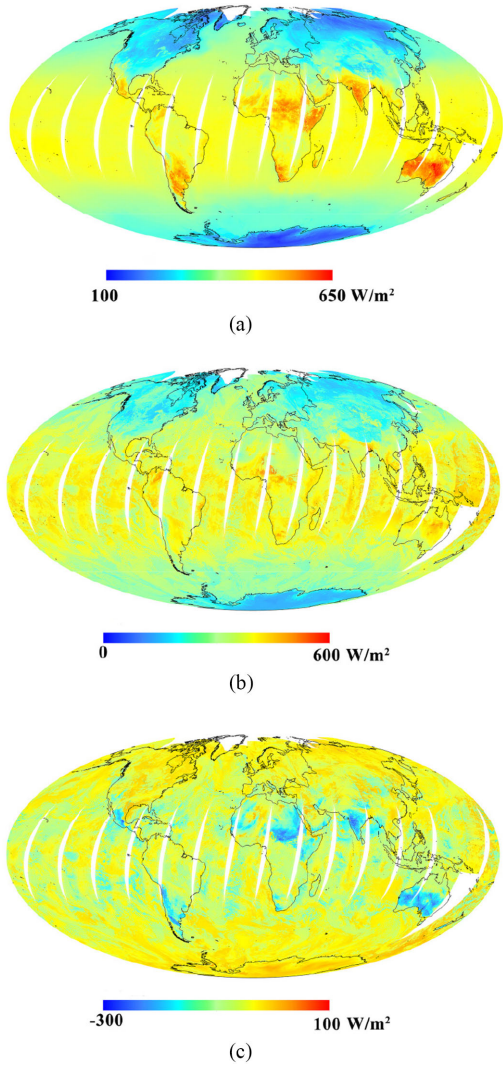

Fig. 3. Examples of global daytime LW radiation maps that were derived from the MODIS/Terra data from DOY 49, 2006. (a) LWUP. (b) LWDN. (c) LWNR.

global maps of GLASS LWUP, LWDN, and LWNR that are produced from the daytime Terra/MODIS data from DOY 49, 2006.

III. Results

As described in Section II-B, the model that is used to estimate cloudy-sky LWDN is a single-layer model [36], which is the same as that adopted by Bisht and Bras [68], and the method for estimating cloudy-sky LWUP is also similar to that used by Bisht and Bras [68] except that we used our GLASS BBE product. According to the validation over large heterogeneous areas, both instantaneous cloudy-sky LWUP and LWDN reached a high accuracy using the Department of Energy's Atmospheric Radiation Measurement (ARM) program within the Southern Great Plains (SGP) in Oklahoma and Kansas, with biases of –0.15 and 0.28 W/m^2 and RMSEs of 16.11 and 19.34 W/m^2, respectively [58]; afterwards, instantaneous LWUP and LWDN for cloudy skies were validated using the same SGP sites as in Bisht and Bras [58] and additional sites from the National Oceanic

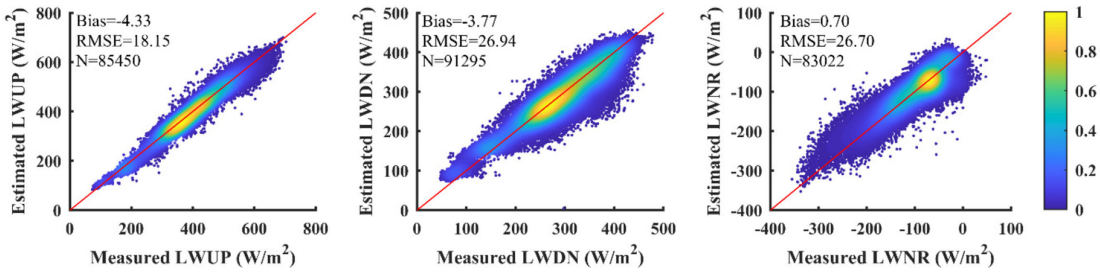

Fig. 4. Overall validation results of GLASS LWUP, LWDN, and LWNR.

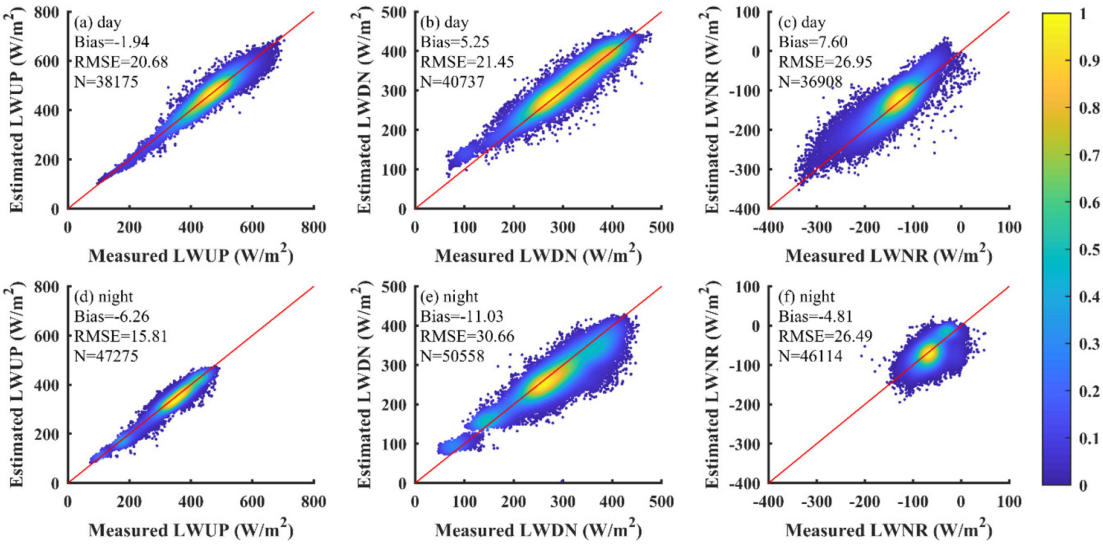

Fig. 5. Validation results of GLASS LWUP, LWDN, and LWNR during daytime and nighttime, respectively.

and Atmospheric Administration's Surface Radiation Budget (SURFRAD) network, with biases of –2.52 and 11.5 W/m^2 and RMSEs of ±24.9 and 36.6 W/m^2, respectively. This study focuses on the validation of the clear-sky LW radiation product. Once we have completed the development of the new cloudy-sky LW radiation algorithms, we will update the GLASS LW radiation product and conduct the validation of the cloudy-sky LW radiation.

To fully assess the performance of the GLASS LW radiation product, the LW radiation products are evaluated under various conditions. MOD11 and MYD11 are used to identify clear-sky pixels over land. A pixel is labeled as the clear sky if the corresponding LST has the highest quality. MOD35 and MYD35 are used to identify clear-sky pixels over the ocean as MODIS did not provide MOD11 or MYD11 over the ocean surface. Moreover, a pixel is identified as a clear-sky pixel only if the pixels in its 3×3 neighborhood are all clear-sky pixels to avoid the potential pollution of cloudy pixels. The temporal matching criterion is that the time difference between the satellite overpass and the site measurement time in one day is less than half the temporal resolution of the site measurements. For example, the time difference must be less than 15 min if the temporal resolution of the site measurements is 30 min. Two indices are used to characterize the accuracy of the GLASS LW radiation product, namely, the bias and the root-mean-square error (RMSE), which are defined as follows:

$$\text{bias} = \frac{1}{N}\sum_{i=1}^{N}(\text{LW}_{\text{ret}} - \text{LW}_{\text{obs}}) \tag{9}$$

$$\text{RMSE} = \text{sqrt}\left(\sum_{i=1}^{N}(LW_{\text{ret}} - LW_{\text{obs}})^2/N\right) \tag{10}$$

where LW_{ret} and LW_{obs} represent the satellite-derived surface LW radiation and the site-measured surface LW radiation, respectively, and N is the number of matched samples.

A. Global Accuracy

In total, we obtained 85 450 samples for LWUP, 91 295 samples for LWDN, and 83 022 samples for LWNR. Not all sites have the measurements of LWUP, and the measurands of LWUP and LWDN are not synchronized. The validation results are presented in Figs. 4–8. We describe the evaluation results in the following. As shown in Fig. 4, the GLASS LW radiation values are satisfactory in accordance with the ground measurements. The samples of LWUP are distributed around 1:1 lines. Both LWDN and LWNR are slightly overestimated when the observed values are small. The biases are –4.33, –3.77, and 0.70 W/m^2, and the RMSEs are 18.15, 26.94, and 26.70 W/m^2 for LWUP, LWDN, and LWNR, respectively. Gui

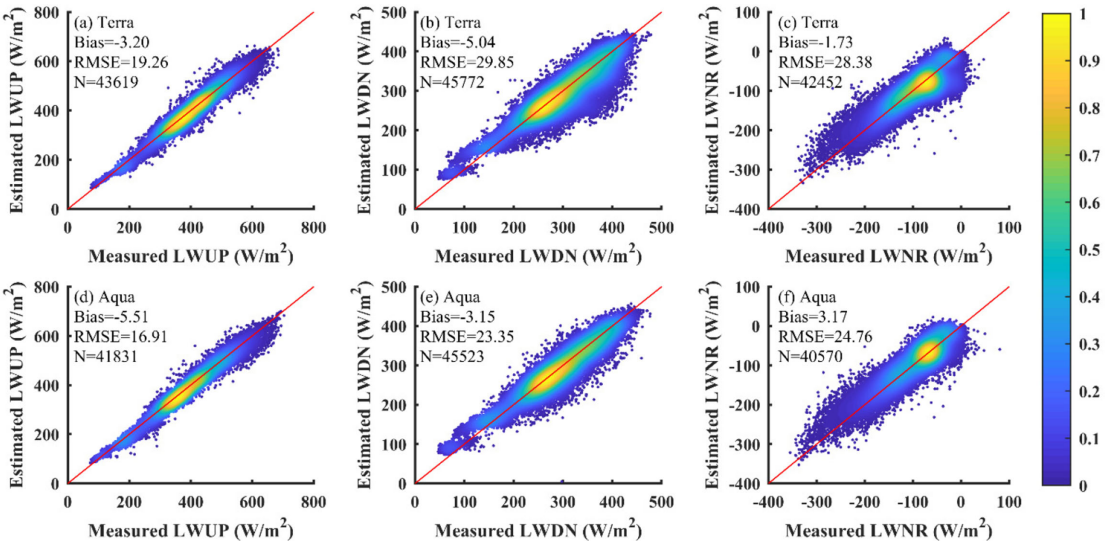

Fig. 6. Accuracies of GLASS LWUP, LWDN, and LWNR derived from Terra and Aqua, respectively.

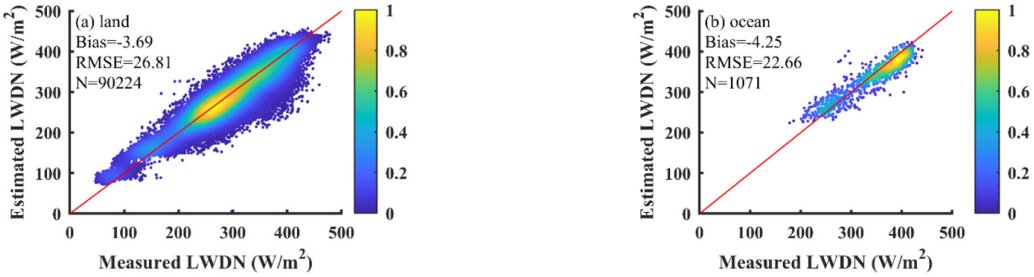

Fig. 7. Accuracies of GLASS LWDN over land and ocean, respectively.

et al. [10] evaluated 3-h (GEWEX-SRB and ISCCP-FD) and instantaneous (CERES-FSW) clear-sky LWUP and LWDN from 15 sites of the SURFRAD, CEOP, and AsiaFlux networks. According to their study, the biases (RMSEs) of GEWEX-SRB, ISCCP-FD, and CERES-FSW are 6.4 (27.9), 10.4 (27.6), and 10.8 (28.8) W/m^2 for LWUP, and 18.8 (21.6), 11.1 (35.2), and 8.1 (18.7) W/m^2 for LWDN, respectively. Our proposed product outperforms GEWEX-SRB, ISCCP-FD, and CERES-FSW, except for LWDN, for which RMSE was large.

Fig. 5 presents the evaluation results and GLASS LW fluxes in the daytime and at the nighttime. The sample distributions of LWUP and LWDN are similar to those in Fig. 4. LWDN is significantly overestimated in the daytime at the lower end of the observed LWDN. The ranges of LWUP and LWNR at the nighttime are narrower than those in the daytime. The biases of LWUP are –1.94. and –6.26 W/m^2, and the RMSEs are 20.68 and 15.81 W/m^2 during the daytime and nighttime, respectively. The biases and RMSE of LWDN in the daytime are 5.25 and 21.45 W/m^2, respectively. LWDN is underestimated with a bias and an RMSE of –11.03 and 30.66 W/m^2, respectively, at the nighttime. The bias of LWNR is positive in the daytime and negative at the nighttime, and the RMSE is less than 27 W/m^2.

Fig. 6 presents the evaluation results of the GLASS LW radiation product from Terra and Aqua. The sample distributions of the LW radiation from Terra are similar to those from Aqua. There is no significant difference between Terra and Aqua in terms of the evaluation results, except that the RMSEs of the LW radiation from Terra are all slightly larger than those from Aqua. The statistical results are presented in Table I. The biases of LWUP are –3.20 and –5.51 W/m^2, and the RMSEs are 19.26 and 16.91 W/m^2 for Terra and Aqua, respectively. The biases of LWDN are –5.04 and –3.15 W/m^2, and the RMSEs are 29.85 and 23.35 W/m^2. The biases of LWNR are –1.73 and 3.17 W/m^2, and the RMSEs are 28.38 and 24.76 W/m^2.

The performances of the GLASS LW radiation product over land and ocean are evaluated, and the results are presented in Fig. 7. Due to a lack of site measurements over the ocean surface, we only obtain four sites with LWDN measurements over the ocean surface. Similar to the evaluation results in Fig. 4, LWDN is overestimated at the lower end of the observed LWDN. The biases of LWDN over land and ocean are –3.69 and –4.25 W/m^2, and the RMSEs are 26.81 and 22.66 W/m^2.

Fig. 8 presents the performance of the GLASS LW radiation product for each independent network. The performance of the GLASS LW radiation product differs among the networks. At the first glance, LWUP outperforms LWDN and LWNR with samples that are distributed in a narrowband that is centered at the 1:1 line. LWUP performs well on each network except AsiaFlux, for which the absolute bias exceeds 10 W/m^2. The

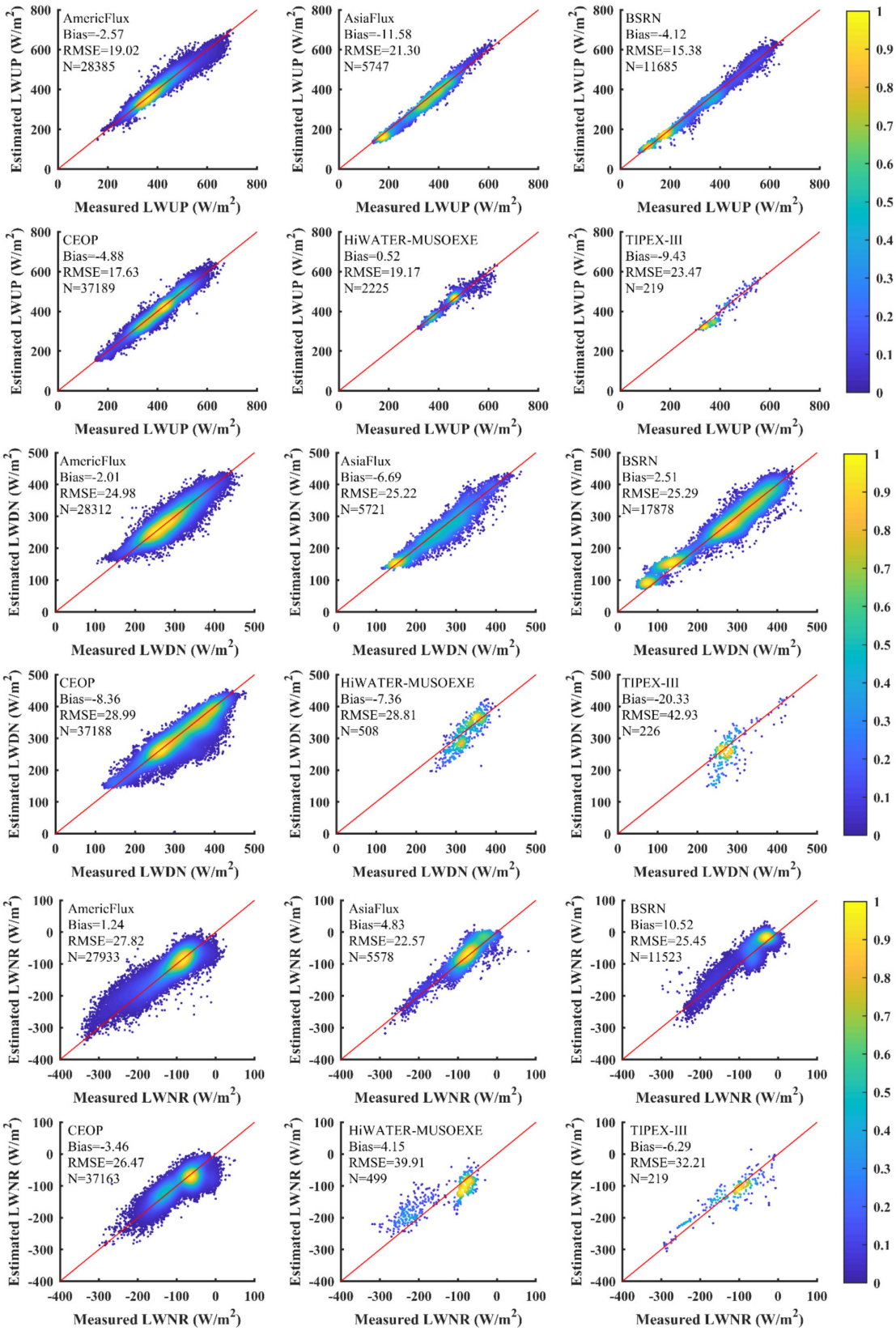

Fig. 8. Validation results of GLASS LWUP, LWDN, and LWNR using the ground measurements collected from six networks.

TABLE I
EVALUATION RESULTS OF THE GLASS LWUP, LWDN, AND LWNR FOR EACH INDEPENDENT NETWORK UNDER THE CLASSIFICATIONS OF DAY AND NIGHT, TERRA AND AQUA, AND LAND AND OCEAN

		Indices (W/m^2)	AmeriFlux	AsiaFlux	BSRN	CEOP	HIWATER-MUSOEXE	TIPEX-III	All networks
Day	LWUP	bias	-1.12	-2.61	-5.80	-2.03	3.83	2.55	-1.94
		RMSE	24.38	18.54	19.45	17.72	23.3	20.46	20.68
	LWDN	bias	4.71	-2.32	12.09	3.54	6.70	11.86	5.25
		RMSE	22.36	23.95	26.93	17.22	23.15	20.73	21.45
	LWNR	bias	7.42	-2.26	19.90	5.60	24.50	10.21	7.60
		RMSE	29.92	21.18	31.04	23.15	49.88	24.21	26.95
Night	LWUP	bias	-3.82	-16.79	-3.19	-7.37	-4.55	-16.06	-6.26
		RMSE	12.70	22.74	12.57	17.55	9.93	24.99	15.81
	LWDN	bias	-7.96	-9.25	-1.87	-18.72	-25.21	-38.31	-11.03
		RMSE	27.09	25.94	25.02	36.2	33.44	51.30	30.66
	LWNR	bias	-4.06	9.19	5.23	-11.36	-17.65	-20.65	-4.81
		RMSE	25.91	23.41	21.56	29.06	28.57	35.36	26.49
Terra	LWUP	bias	-1.57	-10.66	-2.33	-4.04	5.58	-7.67	-3.20
		RMSE	19.12	20.96	15.15	20.11	18.96	27.6	19.26
	LWDN	bias	-0.86	-4.42	2.7	-11.9	-3.42	-13.76	-5.04
		RMSE	24.74	23.74	26.12	35.38	27.61	39.18	29.85
	LWNR	bias	0.86	4.02	9.43	-7.86	-1.5	3.33	-1.73
		RMSE	27.79	20.23	26	30.44	34.36	20.91	28.38
Aqua	LWUP	bias	-3.67	-12.55	-5.74	-5.76	-4.2	-10.86	-5.51
		RMSE	18.92	21.65	15.59	14.58	19.36	19.5	16.91
	LWDN	bias	-3.24	-9.14	2.33	-4.63	-10.43	-25.83	-3.14
		RMSE	25.23	26.73	24.46	20.1	28.46	45.83	23.30
	LWNR	bias	1.66	5.75	11.51	1.15	9.44	-14.09	3.17
		RMSE	27.86	24.97	24.94	21.53	44.47	39.03	24.76
Land	LWUP	bias	-2.57	-11.58	-4.12	-4.88	0.52	-9.43	4.33
		RMSE	19.02	21.30	15.38	17.63	19.17	23.47	18.15
	LWDN	bias	-2.01	-6.69	4.38	-8.36	-7.36	-20.33	-3.69
		RMSE	24.98	25.22	27.02	28.99	28.81	42.93	26.81
	LWNR	bias	1.24	4.83	10.52	-3.46	4.15	-6.29	0.66
		RMSE	27.82	22.57	25.45	26.47	39.91	32.21	26.67
Ocean	LWUP	bias	/	/	/	/	/	/	/
		RMSE	/	/	/	/	/	/	/
	LWDN	bias	/	/	-4.25	/	/	/	-4.25
		RMSE	/	/	22.66	/	/	/	22.66
	LWNR	bias	/	/	/	/	/	/	/
		RMSE	/	/	/	/	/	/	/

absolute bias of LWDN is less than 10 W/m^2, and RMSE is approximately 25 W/m^2, except on TIPEX-III, where the bias is –20.33 W/m^2. The biases of LWNR are all less than 10.52 W/m^2, and RMSE is approximately 30 W/m^2.

To further analyze the evaluation results of various radiation flux networks in this study, the evaluation results are separated into day and night, Terra and Aqua, and land and ocean. Table I presents a statistical summary of the GLASS LW radiation product evaluation results. LWUP realizes satisfactory evaluation results for the six networks during the daytime and nighttime, except that it is underestimated for AsiaFlux and TIPEX-III at the nighttime with biases and RMSEs of –16.79 and 22.74 W/m^2, and –16.06 and 24.99 W/m^2, respectively. LWDN is significantly underestimated at the nighttime. The biases of LWDN are almost all positive in the daytime and negative at the nighttime. LWDN is strongly overestimated for BSRN and TIPEX-III with biases and RMSEs of 12.09 and 26.93 W/m^2, and 11.96 and 20.73 W/m^2, respectively, in the daytime, while it is significantly underestimated for CEOP, HIWATRE-MUSOEXE, and TIPEX-III with absolute values of the bias and RMSE that exceed 18 and 36 W/m^2, respectively, at the nighttime. This may be due to the inaccuracy in the nocturnal CWV that is acquired by resampling the CWV of MOD05_L2/MYD05_L2. The changes in the bias and RMSE of LWNR are similar to those for the LWDN in daytime and nighttime, and LWNR is substantially overestimated in the daytime for BSRN, HIWATER-MUSOEXE, and TIPEX-III with biases of 19.90, 24.50, and 10.21 W/m^2, respectively, and RMSEs of 31.04,

TABLE II
EVALUATION RESULTS OF THE GLASS LWUP, LWDN, AND LWNR UNDER TEN LAND COVER TYPES

Land cover type	No.Site	LW flux	bias(W/m^2)	RMSE(W/m^2)
Barren land	6	LWUP	-8.28	23.72
	6	LWDN	-12.38	33.38
	6	LWNR	-4.07	23.73
Cropland	29	LWUP	-1.17	16.42
	31	LWDN	-7.07	25.68
	29	LWNR	-6.08	27.16
Forest	28	LWUP	-4.35	17.60
	28	LWDN	-3.97	23.90
	28	LWNR	0.53	23.88
Grassland	36	LWUP	-6.30	19.05
	40	LWDN	-4.44	27.68
	36	LWNR	1.68	28.27
Ice/Tundra	7	LWUP	-2.61	11.25
	7	LWDN	17.12	26.68
	7	LWNR	17.71	25.20
Savanna	7	LWUP	6.40	25.84
	7	LWDN	-2.46	31.88
	7	LWNR	-8.43	29.12
Shrubland	3	LWUP	-8.82	14.85
	3	LWDN	-16.19	29.52
	3	LWNR	-7.38	24.22
Urban and Built-up Land	2	LWUP	-16.45	19.63
	12	LWDN	0.05	27.75
	2	LWNR	5.04	19.69
Waterbody(Ocean)	0	LWUP	/	/
	4	LWDN	-4.25	22.66
	0	LWNR	/	/
Wetland	3	LWUP	-7.18	16.03
	3	LWDN	5.02	23.94
	3	LWNR	11.43	31.58

49.88, and 24.21 W/m^2, respectively, while it is underestimated for CEOP, HIWATER-MUSOEXE, and TIPEX-III with absolute biases and RMSEs that exceed 11.36 and 28.57 W/m^2. It is inferred that LWDN is the main contribution to LWNR.

There is no significant discrepancy between Terra and Aqua for AmeriFlux, AsiaFlux, and BSRN. The bias of LWUP is positive for Terra while negative for Aqua for HIWATER-MUSOEXE. The bias discrepancy of LWDN is more than 7 W/m^2 in CEOP, HIWATER-MUSOEXE, and TIPEX-III, and the RMSEs are 35.38, 27.61, and 39.18 W/m^2, respectively, from Terra and 20.01, 28.46, and 45.83 W/m^2, respectively, from Aqua. Combined these results, LWNR also shows significant discrepancies between Terra and Aqua: for the three networks, the biases are –7.06, –1.5, and 3.33 W/m^2 for Terra, and the corresponding RMSEs are 30.44, 34.36, and 20.91 W/m^2, compared to biases of 1.15, 9.44, and –14.09 W/m^2 for Aqua, with corresponding RMSEs of 21.53, 44.47, and 39.03 W/m^2. The large offset between the two satellite platforms may be caused by the discrepancies in satellite calibration [69].

B. *Effect of the Land Cover Type*

The land cover type is the main factor that regulates earth–atmosphere interactions [70]. We investigate the performance of the GLASS LW radiation product for various land cover types. The site land cover types are aggregated into ten types, namely, barren land, cropland, forest, grassland, ice/tundra, savanna, shrubland, urban and built-up land, waterbody, and wetland, according to the classification of the International Geosphere-Biosphere Program (IGBP). Among them, four ocean sites are classified into the waterbody class, for which only LWDN was measured; the barren land class is composed of desert and barren land (only Ali). The number of sites for each land cover type is specified in Table II.

Fig. 9 presents the evaluation results of the GLASS LWUP product under the ten land cover types. LWUP performs well for all the land cover types. The statistical results are summarized in Table II. The absolute values of the bias are all less than 8.82 W/m^2, except for the urban and built-up lands class, which has few extracted samples. All RMSEs are approximately 20 W/m^2. LWUP is significantly underestimated, although its RMSE is less than 20 W/m^2 for urban and built-up lands. This may be due to the typical urban climate phenomena, such as the urban heat island, that are found throughout the day and can increase the surface temperature, and radiation in the street geometry, such as street canyons, also affects LWUP significantly [71], [72]. Moreover, urban land types are complex, for example, due to plants and buildings, the spatial variability of which can lead to significant differences in heat fluxes, which give rise to

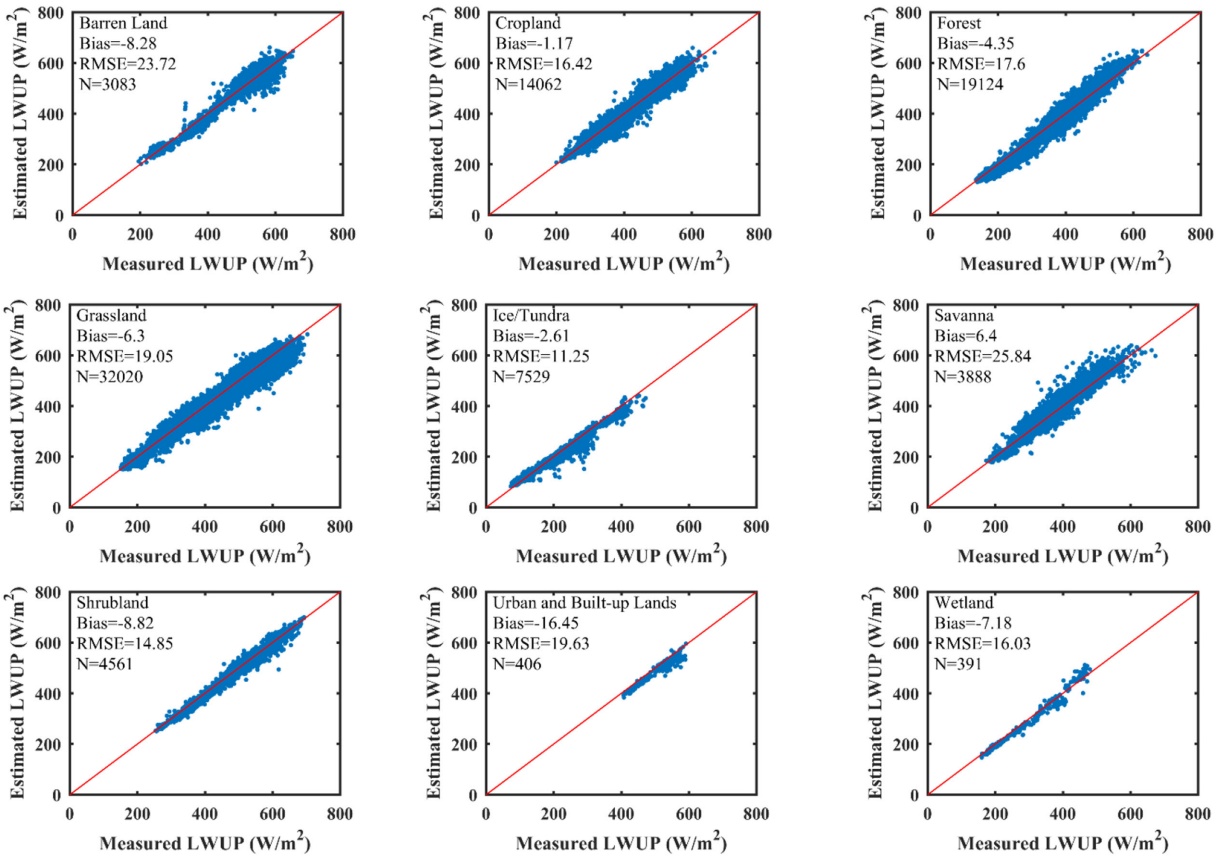

Fig. 9. Comparison between GLASS LWUP and site measured LWUP under ten land cover types.

observable local climate effects that produce spatial variability in LW radiation [72], [73]. The bias and RMSE are –4.25 and 22.66 W/m^2, respectively, for the ocean class.

The evaluation results of the GLASS LWDN product are presented in Fig. 10. Visually, the points are evenly distributed around the equinoctial line with the exception of barren land. The LWDN for barren land is significantly underestimated when the measured LWDN is approximately 200–400 W/m^2, which is mainly due to the nighttime sample. That is because LWUP, as an input parameter, is also underestimated in that range at the nighttime. The nocturnal water vapor quality may be another reason. According to Table II, the statistical data of the bias and RSME demonstrate that LWDN is substantially overestimated over ice/tundra and underestimated over shrubland, except the performance of satellite-derived LWDN is better, with a bias range from –7.07 to 5.02 W/m^2 and a corresponding RMSE range from 22.66 to 27.68 W/m^2.

Fig. 11 presents the evaluation results of the GLASS LWNR product under the ten land cover types. At first glance, the points are evenly distributed on both sides of the 1:1 line, except for the ice/tundra and urban and built-up lands. The LWNR is substantially overestimated when LWNR is approximately –200–$-$100 W/m^2, with a bias and an RMSE of 5.01 and 19.69 W/m^2, respectively, for the urban and built-up land, because LWUP is underestimated at the same time. LWNR is overestimated with a bias and an RMSE of 17.71 and 25.20 W/m^2, respectively, for ice/tundra due to the overestimation of the LWDN. As presented in Table II, except for these two types of land covers and wetlands, the biases of all cover types range from –8.43 to 5.04 W/m^2.

C. *Effect of the Surface Elevation*

The LW radiation is closely related to the air temperature and the water vapor, which are the driving factors behind the vertical zonality. Furthermore, the surface elevation is a direct quantitative indicator of the vertical zonality [32]. In this study, surface elevations are divided into four intervals ($<$500 m, 500–1000 m, 1000–3000 m, and $>$3000 m). The GLASS LW radiation product is evaluated under various surface elevations. The number of sites for each surface elevation interval is specified in Table III. Fig. 12 shows scatterplots between the GLASS LW radiation and the observed LW radiation. LWUP performs well in the four surface elevation ranges. When the surface elevation exceeds 3000 m, the performances of LWDN and LWNR degrade. The statistical results are presented in Table III. The bias of LWUP ranges from –4.96 to 1.32 W/m^2, and the RMSE values are less than 18.32 W/m^2; hence, LWUP is only slightly affected by the surface elevation, and LWUP performs well under various surface elevations. In contrast, LWDN responds differently to elevations that exceed 3000 m than to elevations in the other three surface elevation intervals. LWDN is overestimated when LWDN is less than 200 W/m^2. This because LWDN is sensitive to the water vapor at high elevations, especially when the water

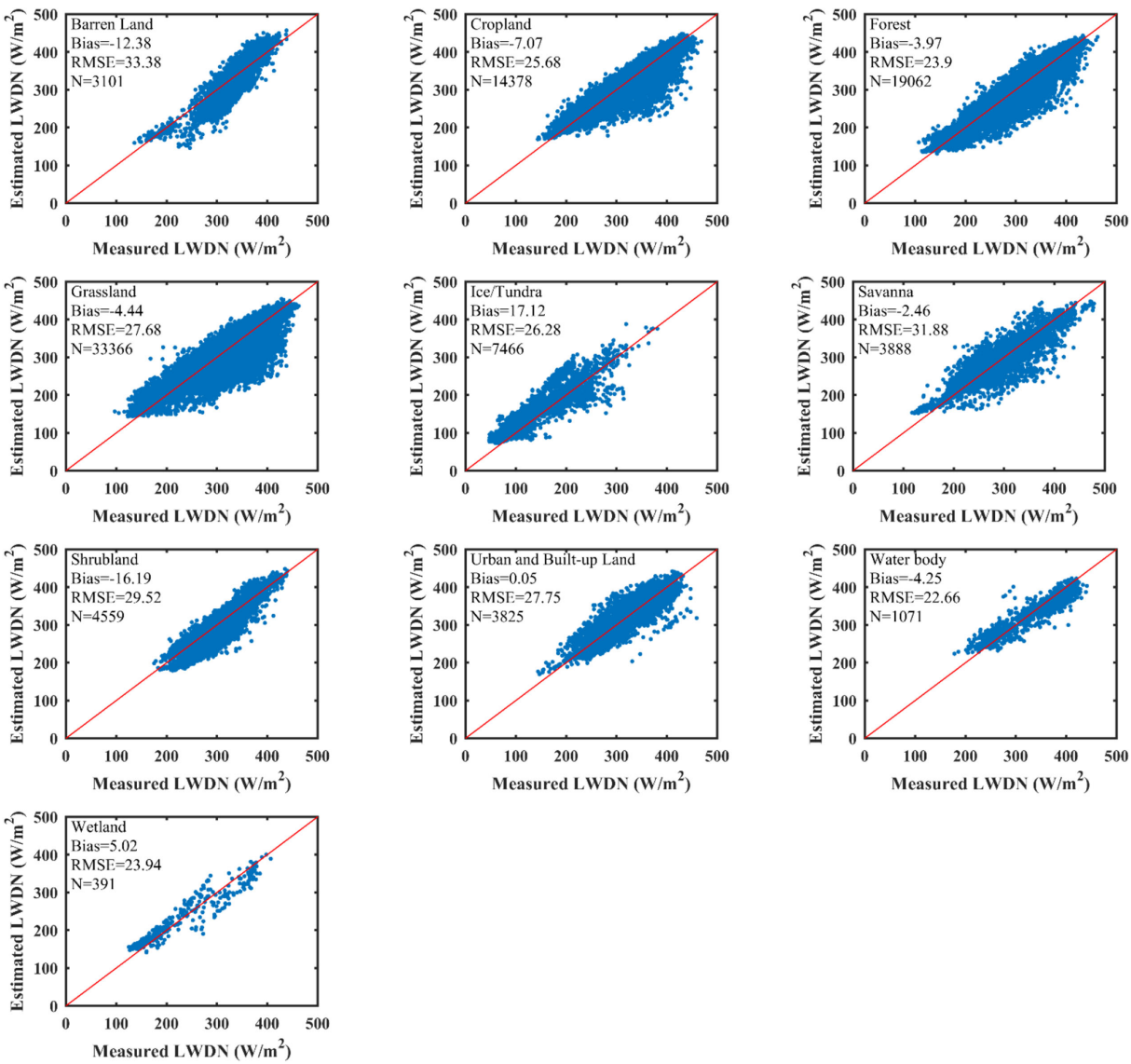

Fig. 10. Comparison between GLASS LWDN and site measured LWDN under ten land cover types.

TABLE III
EVALUATION RESULTS OF THE GLASS LWUP, LWDN, AND LWNR UNDER VARIOUS SURFACE ELEVATIONS

surface elevation	No.Site	LW flux	bias(W/m^2)	RMSE(W/m^2)
<500m	64	LWUP	-4.96	18.32
	81	LWDN	-3.19	22.09
	64	LWNR	0.07	26.09
500-1000m	12	LWUP	-5.15	16.55
	12	LWDN	-4.73	23.31
	12	LWNR	1.78	25.94
1000-3000m	33	LWUP	-0.73	16.67
	35	LWDN	-2.26	26.94
	33	LWNR	0.36	29.28
>3000m	12	LWUP	1.32	12.84
	13	LWDN	15.34	26.99
	12	LWNR	14.16	27.67

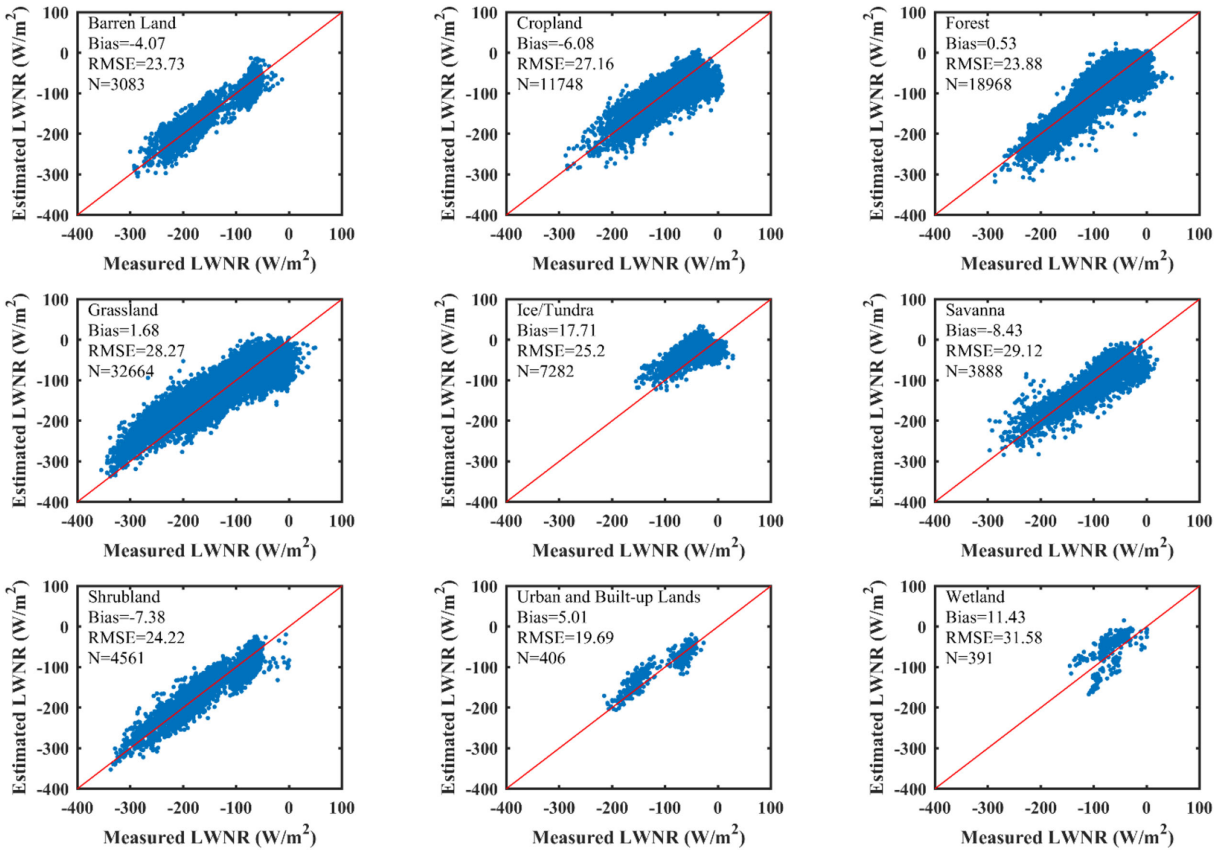

Fig. 11. Comparison between GLASS LWNR and site measured LWNR under ten land cover types.

vapor is very low [55], [74]. The bias of LWNR is similar to that of LWDN when the surface elevation exceeds 3000 m. The biases at the other surface elevations are 0.07, 1.78, and 0.36 W/m^2. The RMSEs of LWNR are slightly larger than those of LWDN.

D. Effect of the Climatic Type

The surface LW radiation is closely related to LST, the screen-level air temperature and CWV, among other factors. The primary criteria for the climatic-type classification are the temperature and the precipitation [32]. The climatic type may affect the performance of the surface LW radiation product. For example, LWDN is prone to be overestimated due to low CWV [33]. Thus, we evaluated the performance of the GLASS LW radiation product for each climatic type in the Koppen climate classification, which was classified based on the vegetation types of a region, together with the temperature and the precipitation [75]. The sites are of 16 climatic types: af (tropical, rainforest), aw (tropical, savannah), bsh (arid, steppe, hot), bsk (arid, steppe, cold), bwh (arid, desert, hot), bwk (arid, desert, cold), cfa (temperate, no dry season, hot summer), cfb (temperate, no dry season, warm summer), csa (temperate, dry summer, hot summer), csb (temperate, dry summer, warm summer), dfa (cold, no dry season, hot summer), dfb (cold, no dry season, warm summer), dfc (cold, no dry season, cold summer), dfd (cold, no dry season, very cold winter), dwa (cold, dry winter, hot summer), and et (polar, tundra, or frost). The number of sites for each climatic type is specified in Table IV. Next, evaluations are conducted for various climatic types.

Fig. 13 compares LWUP versus the observed LWUP for 15 climatic types. The statistical results are presented in Table IV. LWUP performs well with bias ranges from –8.75 to –0.13 W/m^2 and RMSE ranges from 10.90 to 20.64 W/m^2 with the exception of climatic types csa and dfd. The biases are approximately –20 W/m^2 and the RMSEs exceed 25 W/m^2 for climatic types csa and dfd. Csa and dfd are special climate types. Csa is Mediterranean climate, which has a dry and hot summer and a rainy winter. Such atmospheric profiles may not be fully considered in the development of the LWUP algorithm. Dfd is wet year-round, and the cloud identification represents the average of a pixel, while the measured value represents only a point; hence, the low accuracy of LWUP may be due to the cloud contamination.

The evaluation results of LWDN are presented in Fig. 14. LWDN is consistent with the observed LWDN. The statistical results are presented in Table IV. The bias ranges from –11.04 to 1.76 W/m^2, and RMSE ranges from 18.33 to 31.76 W/m^2, with the exception of climatic types aw, bwh, and et. The corresponding bias and RMSE are approximately $\pm$15 and 30 W/m^2, respectively. Aw is a tropical wet and dry or savanna climate, and seasonal differences in terms of water vapor may be lead to the low accuracy of LWDN; the low accuracy of nocturnal

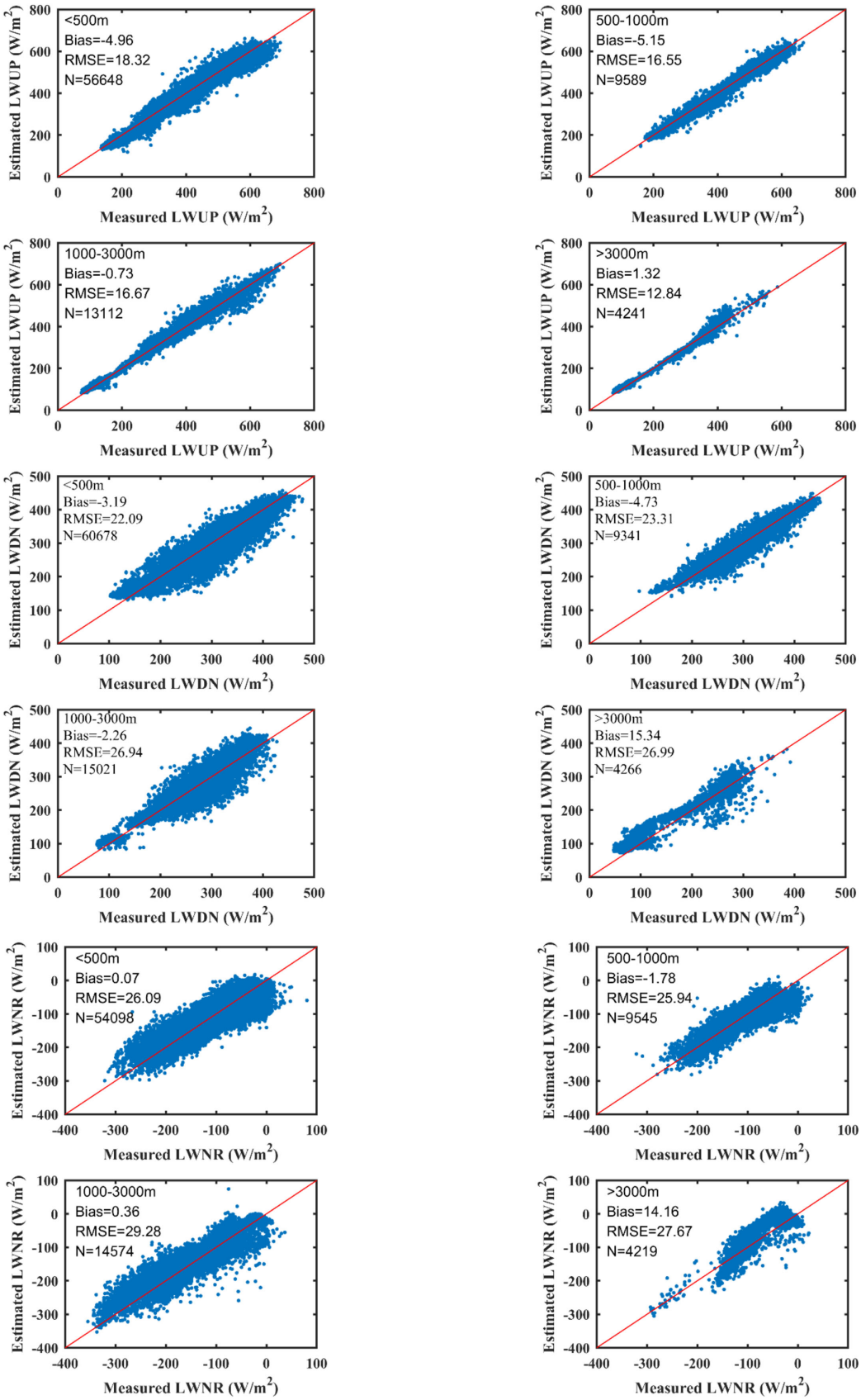

Fig. 12. Comparison between GLASS derived and site measured LWUP, LWDN, and LWNR under various surface elevations, respectively.

TABLE IV
EVALUATION RESULTS OF THE GLASS LWUP, LWDN, AND LWNR FOR VARIOUS CLIMATIC TYPES

climatic type	No.Site	LW flux	bias(W/m^2)	RMSE(W/m^2)
	4	LWUP	-3.60	16.20
af	7	LWDN	-9.78	23.86
	4	LWNR	0.70	30.26
	3	LWUP	-8.75	19.20
aw	5	LWDN	-13.91	27.08
	3	LWNR	-9.20	27.15
	0	LWUP	/	/
bsh	1	LWDN	-9.54	27.18
	0	LWNR	/	/
	6	LWUP	-0.72	20.64
bsk	6	LWDN	0.78	28.72
	6	LWNR	2.63	28.43
	2	LWUP	-7.80	19.93
bwh	2	LWDN	-17.38	33.14
	2	LWNR	-9.66	23.20
	20	LWUP	-0.13	19.64
bwk	20	LWDN	-10.02	31.76
	20	LWNR	0.44	37.43
	20	LWUP	-3.09	16.63
cfa	23	LWDN	-5.73	28.99
	20	LWNR	-3.60	26.53
	3	LWUP	-5.57	10.90
cfb	6	LWDN	-4.43	22.07
	3	LWNR	-4.36	26.62
	2	LWUP	-23.55	33.43
csa	2	LWDN	-3.81	19.22
	2	LWNR	17.78	36.82
	5	LWUP	-1.73	18.77
csb	5	LWDN	-0.12	22.71
	5	LWNR	1.28	27.97
	16	LWUP	-2.16	16.78
dfa	17	LWDN	-8.02	27.96
	17	LWNR	-5.54	26.80
	11	LWUP	-5.74	16.00
dfb	12	LWDN	-2.46	19.52
	11	LWNR	2.06	22.26
	5	LWUP	-5.25	18.69
dfc	5	LWDN	1.76	26.99
	5	LWNR	3.45	25.96
	2	LWUP	-19.11	25.51
dfd	2	LWDN	-11.04	22.76
	2	LWNR	6.78	21.15
	2	LWUP	-8.75	16.20
dwa	2	LWDN	0.46	18.33
	2	LWNR	9.21	22.81
	18	LWUP	-4.67	13.57
et	19	LWDN	11.64	27.68
	18	LWNR	17.76	25.37

LWDN with a bias and an RMSE of –27.18 and 36.28 W/m^2, respectively, is the main contributor to the underestimation for bwh, compared to –0.96 and 24.04 W/m^2 in daytime. Bsh is desert climate that is dry and hot, and the underestimation of LWDN over dry and hot regions may be a result of the surface strong cooling effect without high surface insolation at the nighttime. The reasons for the overestimation of LWDN for et are complicated, e.g., the overestimation may be due to high elevation with low water vapor (TIPEX-III), as described in Section III-C, while other sites at the continental boundary have only low vapor, and the air temperature is also affected by the ocean, while the surface temperature is very low. Although the performance of LWDN is slightly worse for several climatic types, LWDN performs better for cfb, csa, csb, dfc, and dwa with biases from –4.43 to 1.76 W/m^2 and RMSEs of less than 22.71 W/m^2.

Table IV presents the detailed evaluation results of LWNR. The accuracy of LWNR depends on those of LWDN and LWUP.

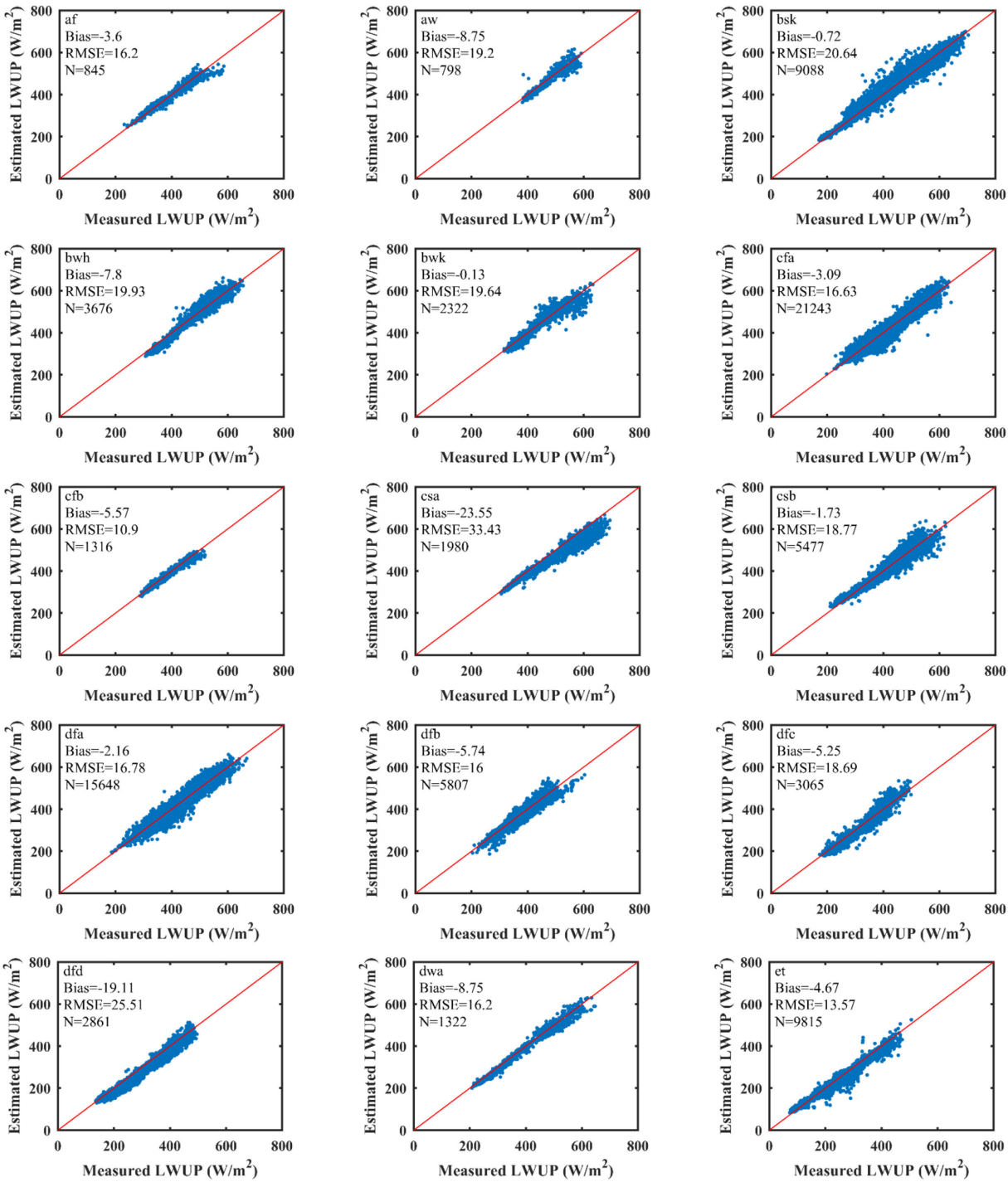

Fig. 13. Comparison between GLASS LWUP and site measured LWUP under various climatic types.

The absolute values of the biases between LWUP and LWDN, except for csa and et, range from 0.44 to 9.21 W/m^2. The RMSEs are approximated by the larger RMSEs between LWUP and LWDN, which range from 21.15 to 37.43 W/m^2. LWNR is overestimated for csa because LWUP is significantly underestimated with a bias of –23.55 W/m^2 and an RMSE of 33.43 W/m^2, while the performance of LWDN is satisfactory with a bias of –3.81 W/m^2 and an RMSE of 19.22 W/m^2. Moreover, due to the negative bias (–4.76 W/m^2) of LWUP and the substantial overestimation (11.64 W/m^2) for LWDN, LWNR is overestimated for et. The results for LWUP over csa and for LWDN over et were discussed earlier in this section. According to the two cases that are discussed above, LWNR is likely to be overestimated if LWUP is significantly underestimated while the corresponding LWDN has a positive bias or LWDN is substantially overestimated while LWUP has a negative bias;

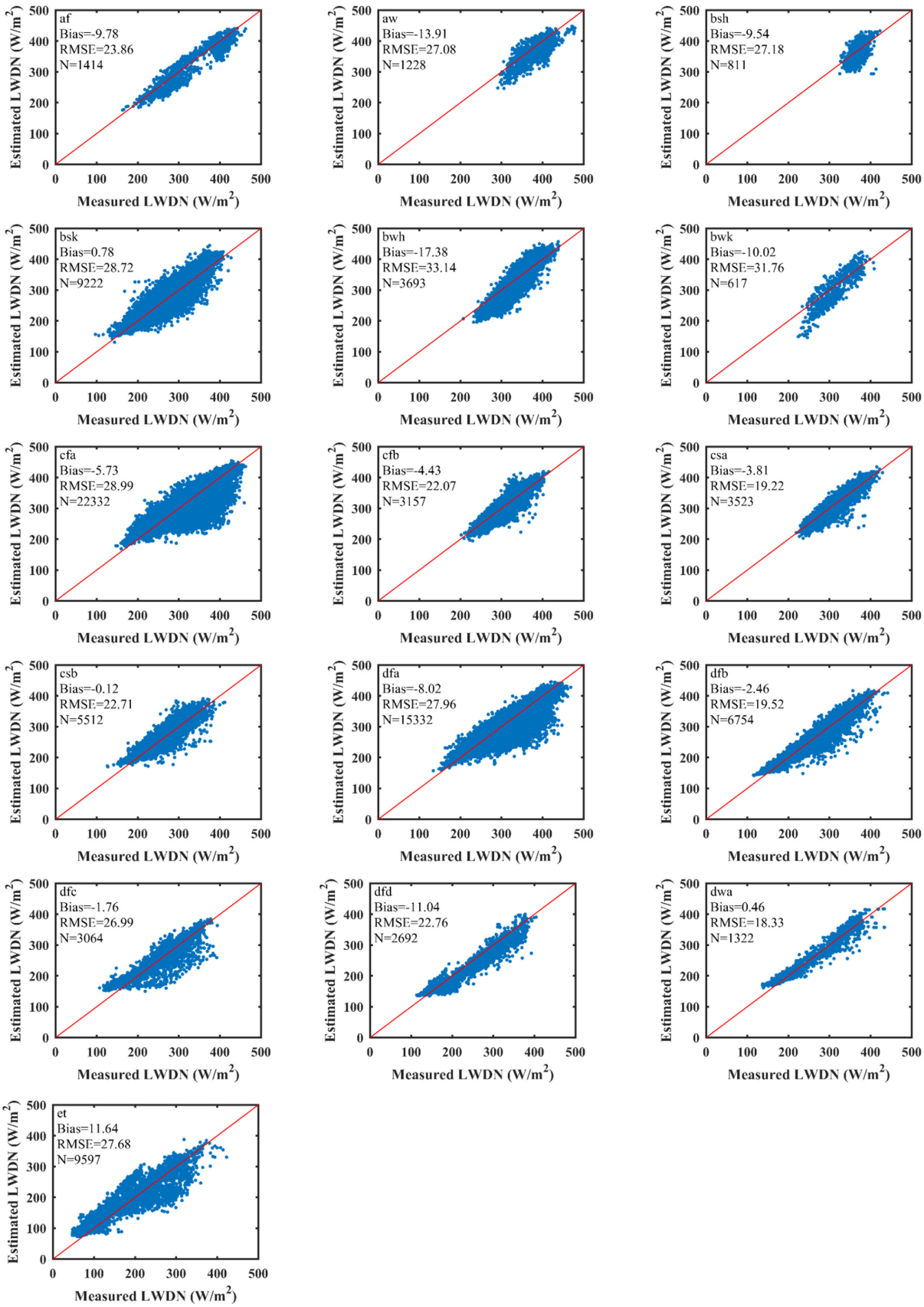

Fig. 14. Comparison between GLASS LWDN and site measured LWDN under various climatic types.

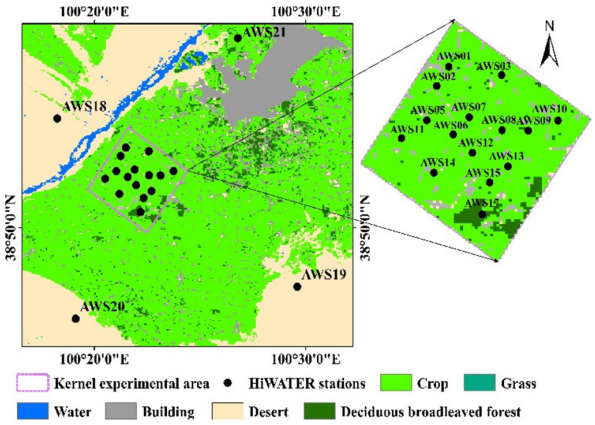

Fig. 15. Site distribution map of the HiWATER-MUSOEXE experiment.

TABLE V
COMPARISON BETWEEN THE EVALUATION RESULTS WITH AVERAGED OBSERVATIONS AND THE AVERAGED ACCURACIES FROM EACH SITE IN A 5.5 km × 5.5 km AREA

	average observation		average accuracy	
	Bias (W/m^2)	RMSE (W/m^2)	Bias (W/m^2)	RMSE (W/m^2)
LWUP	7.90	10.49	3.96	15.42
LWDN	-13.86	14.89	-21.72	30.78
LWNR	21.75	22.81	24.72	33.77

and the accuracy of LWNR depends on the accuracies of LWUP and LWDN.

IV. DISCUSSION

A. *Effect of Surface Spatial Heterogeneity*

The heterogeneity of the land cover can contribute to the satellite-derived LW radiation errors. The HiWATER-MUSOEXE sites are distributed in the typically heterogeneous land surfaces in the middle reaches of the Heihe River Basin. The HiWATER-MUSOEXE dataset (AWS01 to AWS17) was obtained from 17 sites in the 5.5 km × 5.5 km kernel experimental area, which was designed to match the 1 km × 1 km MODIS pixels [61]. The observations in the 5.5 km × 5.5 km kernel experimental area are averaged to obtain a virtual observation, which is used to evaluate the GLASS LW radiation product in this study. As shown in Fig. 15, there is one vegetable site (AWS01), one orchard site (AWS17), and 13 maize sites in the 5.5 km × 5.5 km area.

To assess the effects of the surface spatial heterogeneity, we employ two methods. One is extract LWUPs, LWDNs, and LWNRs from GLASS LW radiation product and ground measurements for each site, then calculated the bias and RMSE using the values averaged over all sites. The other is calculate the bias and RMSE of LWUP, LWDN, and LWNR for each site, then average the calculated biases and RMSEs over all sites. According to Table V, with the first evaluation method, the biases and RMSEs are –7.90 and 10.49 W/m^2, –13.86 and 14.89 W/m^2, and 21.75 and 22.81 W/m^2 for LWUP, LWDN, and LWNR, respectively. With the second method, the biases and RMSEs are –3.96 and 15.42 W/m^2, –21.72 and 30.78 W/m^2, and 24.72 and 33.77 W/m^2 for LWUP, LWDN, and LWNR, respectively. The difference between the two validation methods is significant. Hence, the surface spatial heterogeneity impacts the evaluation results of the LW radiation product.

B. *Performance in Climate Change-Sensitive Areas*

1) Poleward Areas: According to Zhang *et al.* [48], there are larger uncertainties in the GEWES SRB LW radiation in the polar regions. According to their validation results, the bias/RMSE of the three hourly mean GEWES SRB LWDN data that were derived using the GEWEX LW (GLW) and the Langley parameterized LW (LPLA) algorithms were 2.97/35.86 and 3.14/28.18 W/m^2, respectively, in polar regions. Kratz *et al.* (2010) reported that the bias/RMSE of clear-sky LWDN estimated by CERES model A in the polar regions are –11.1/15.3. and –15.2 /12.9 W/m^2 for Terra and Aqua, while the values of the LWDN estimated by CERES model LAPA are –8.3/15.0 and –9.0 /12.4 W/m^2, respectively. In this study, the poleward area is defined as 60°N northward and 60°S southward. Seven BSRN sites (ALE, BAR, DOM, GVN, LER, SPO, and TIK), two AsiaFlux sites (YLF and YPF), two CEOP sites (Barrow and Atqus), and one AmeriFlux site (IVO) are located in poleward areas. The corresponding measurements are used to evaluate the GLASS LW radiation product. Fig. 16 compares the LW radiation with the observed LW radiation in poleward areas. The range of the LW radiation is narrower at the nighttime than that in the daytime. All the points are grouped tightly around the 1:1 line. The biases and RMSEs are –7.42 and 17.09 W/m^2 for LWUP; 5.46 and 24.96 W/m^2 for LWDN; and 13.37 and 24.67 W/m^2 for LWNR, respectively. In summary, the accuracy of GLASS LWDN is comparable to that of GEWES SRB LWDN. Our LW radiation product is an instantaneous product, while GEWES SRB LWDN is a three-hour average product.

Fig. 17 presents the LW validation results of DOM, GVN, and SPO at the Antarctic pole. LWUP performs well with a bias of –0.85 W/m^2 and an RMSE of 11.30 W/m^2 during the day, and a bias of 3.12 and an RMSE of 10.06 W/m^2 at night. LWDN is substantially overestimated at the lower end, especially during the daytime in Fig. 16. This can be largely traced back to the data points of three sites (DOM, GVN, and SPO) at the Antarctic pole. As shown in Fig. 17, the satellite-derived LWDN fluxes visibly exceed the surface-measured fluxes by an average bias of 35.34 W/m^2 during the day, compared to 11.13 W/m^2 at the nighttime. The LWDN in the arctic region is calculated via (3).

For three arctic sites, approximately 75% of the CWV values are less than 0.1 g/cm^2, of which 87% are less than 0.5 g/cm^2 during the day, and approximately 83% of the CWV values are less than 0.1 g/cm^2, of which 100% are less than 0.5 g/cm^2 during the night. These extreme conditions are not incorporated into the developed backup algorithm (3), which may have caused the larger error in the estimated LWDN. The air temperature is also a vital parameter for estimating LWDN, and LWUP is a surrogate for the air temperature in the developed hybrid algorithm for clear-sky LWDN [54], [55]. The Antarctic air temperature is

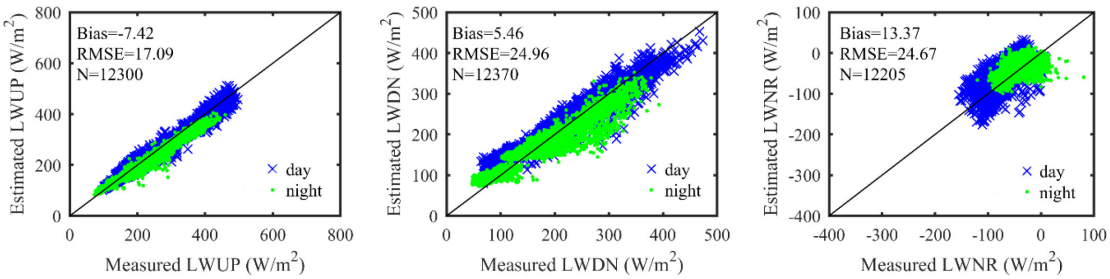

Fig. 16. Evaluation results of GLASS LWUP, LWDN, and LWNR using site measurements in the poleward area, respectively.

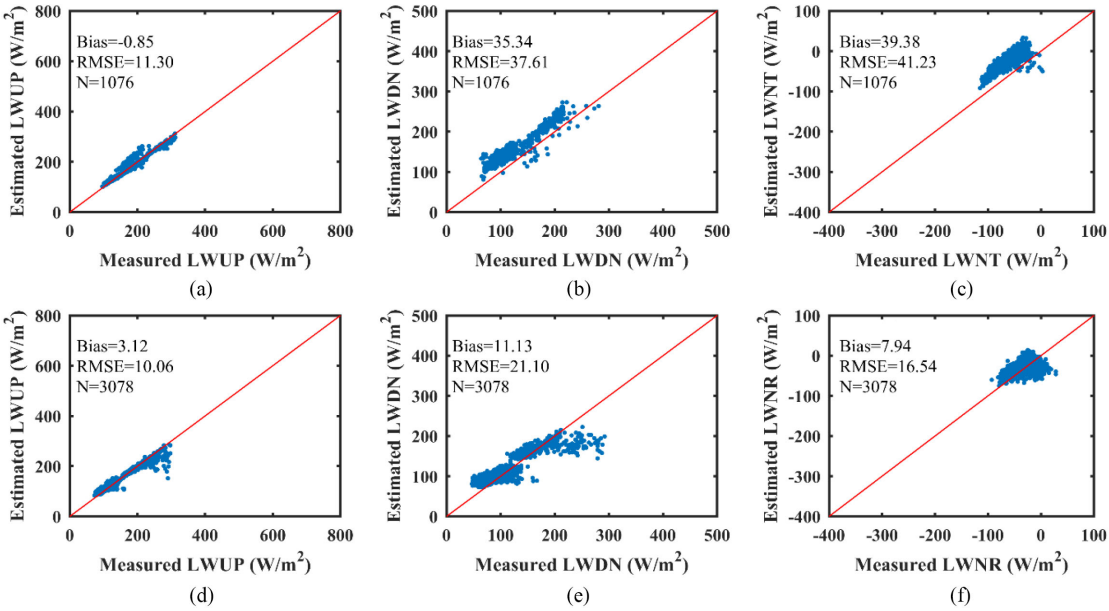

Fig. 17. Comparison between the GLASS derived and site measured LWUP, LWDN, and LWNR at sites DOM GVN and SPO in the Antarctic region, respectively.

strongly affected by the Antarctic climate change and other environmental factors, such as high elevation, ice cover, sea breeze, and the southern hemisphere circulation [76]–[78], which is complicated; hence, LWUP could not accurately represent the air temperature. Therefore, further studies are required for the identification of the uncertainties so that more accurate algorithms can be developed for estimating polar LWDN fluxes and improving the GLASS LW product. LWNR is also significantly overestimated during the daytime with a bias of 39.38 W/m^2 and an RMSE of 41.23 W/m^2. The performance of LWUP is highly satisfactory, while that of LWDN is not satisfactory during the day; thus, the lower accuracy of LWNR is the result of the severe overestimation and the large RMSE of LWDN, and the effect of the LWUP accuracy on LWNR is small. LWNR performs well at night with a bias of 7.94 W/m^2 and an RMSE of 16.54 W/m^2 due to the satisfactory accuracies of both LWUP and LWDN. According to these results, the accuracy of LWNR depends on the accuracies of both LWUP and LWDN, and the LWNR accuracy will not be satisfactory if LWUP and LWDN perform poorly.

2) Semiarid Areas: A semiarid land surface, especially in the mid-latitudes of the Northern and Southern Hemispheres, is one of the most sensitive regions to climate change [49], [77]. Sites PTR, KBU, Aud, Fpe, Ses, and Whs are located in semiarid areas. We evaluated the GLASS LW radiation product over semiarid areas with these sites. The evaluation results are presented in Fig. 18. The statistical results are presented in Table VI The biases and RMSEs are –0.72 and 20.60 W/m^2 for LWUP; –0.37 and 28.62 W/m^2 for LWDN; and 2.63 and 28.43 W/m^2 for LWNR, respectively.

Yan *et al.* [49] validated the CERES SSF instantaneous LW product using the sites at Loess Plateau. Table VI compares the GLASS LW radiation results and the validation results of Yan *et al.* [49] in semiarid regions. The Terra- and Aqua-derived LWUPs differ from their measured values by –67.4 and –44.0 W/m^2 during the day, respectively, and the standard deviations (SDs) are 27.7 and 28.9 W/m^2, while our LWUP differs from their values by 2.51 and –0.84 W/m^2, and the corresponding SDs are 26.76 and 22.04 W/m^2, respectively. At the nighttime, our LWUP is compared with CERES SSF in terms

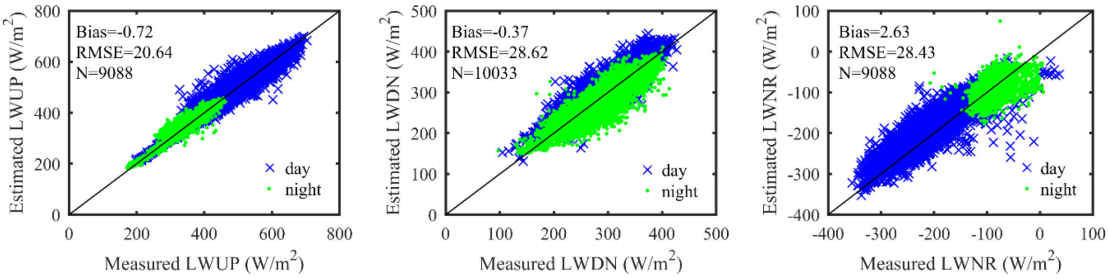

Fig. 18. Evaluation results of GLASS LWUP, LWDN, and LWNR using the site measurements in semiarid areas, respectively.

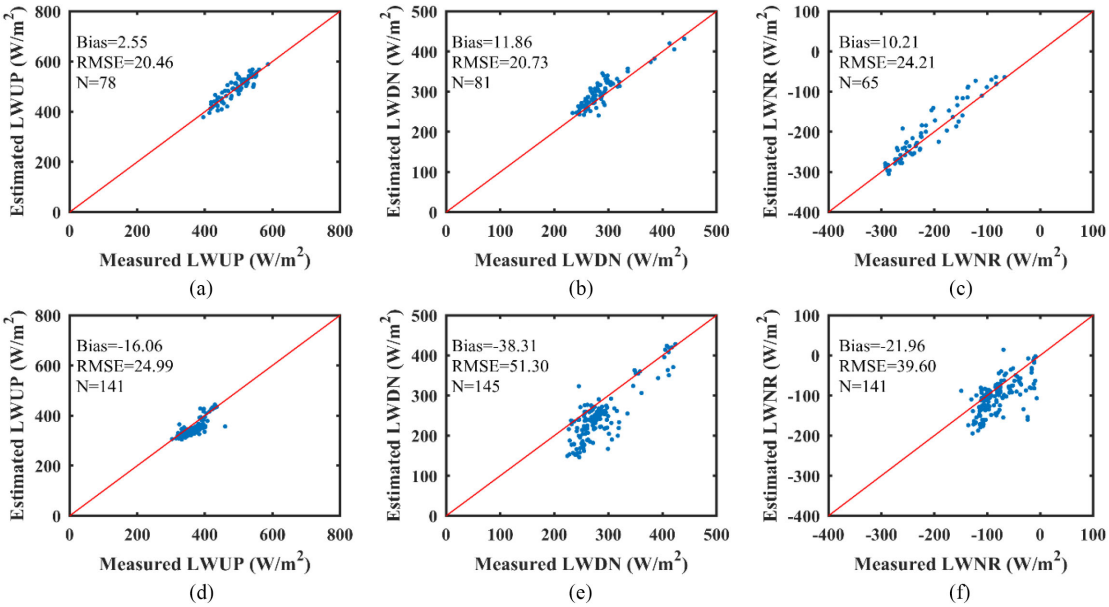

Fig. 19. Evaluation results of GLASS LWUP, LWDN, and LWNR using the site measurements in the Tibetan Plateau, respectively.

TABLE VI
COMPARISON OF THE EVALUATION RESULTS BETWEEN THE GLASS LW RADIATION RESULTS AND THE VALIDATION RESULTS OF YAN et al. (2011) IN SEMIARID AREAS

		Day		Night	
		bias(W/m^2)	SD(W/m2)	bias(W/m2)	SD(W/m2)
LWUP	Terra	2.51(-67.4)	26.76(27.7)	-2.28(-6.9)	16.12(12.0)
	Aqua	-0.84(-44.0)	22.04(28.9)	-2.20(-4.7)	15.72(12.9)
LWDN	Terra	16.99(-0.5)	22.62(10.0)	-13.03(-14.1)	25.93(9.8)
	Aqua	11.94(1.8)	23.05(13.5)	1.93(-15.6)	31.05(12.9)
LWNR	Terra	15.43(-)	28.27(-)	-8.93(-)	24.10(-)
	Aqua	14.71(-)	25.84(-)	-8.29(-)	24.79(-)

The values in parentheses are the results of Yan *et al.* (2011).

of accuracy. The comparison results demonstrate that our LWUP product outperforms the CERES SSF instantaneous LW product in semiarid regions.

LWDN and LWNR are significantly overestimated during the day while slightly underestimated during the night. The biases and SDs are 16.99 and 22.62W/m^2 from Terra and 11.94 and 23.00 W/m^2 from Aqua during the day, and –13.03 and 25.93 W/m^2 from Terra and 1.93 and 31.05 W/m^2 from Aqua at night, respectively. Compared with Yan *et al.* [49], according to which the Terra- and Aqua-derived LWDN differ from their measured values by –0.5 and 0.8 W/m^2 during the day with SDs of 10.0 and 13.5 W/m^2, and by –14.1 and –15.6 W/m^2 at night with SDs of 9.8 and 12.9 W/m^2, our LWDN product is slightly outperformed by the CERES SSF instantaneous LW product in semiarid regions. The overestimation of LWDN in semiarid regions may occur for a similar reason to dry-arid regions,

namely, excessive heating of the surface during times of high surface insolation [50], [79]. The underestimation of LWDN at night may occur because the air temperature decreases faster than the surface temperature in semiarid regions. The GLASS LWNRs from Terra and Aqua differ from the measured values by 15.43 and 14.71 W/m^2 with SDs of 28.27 and 25.84 W/m^2 during the day, compared to differences of –8.93 and –8.29 at night with RMSEs of 24.10 and 24.79 W/m^2, which are due to joint effect of the LWUP and LWDN precisions. The biases for LWDN and LWNR may be negative because without the MODIS visible channel at night, it is difficult to detect low clouds; hence, cloudy scenes may be identified as clear [49]. Less has been reported on the accuracy of LWNR, and the accuracy of our LWNR product may be used as a reference when other researchers must use the dataset directly.

3) Tibetan Plateau: The Tibetan Plateau is known as the "third pole" and has a high elevation of more than 4500 m. This unique region significantly influences the water cycles and climate changes at local and global scales. LW radiation acts as an important index for the investigation of water cycles and climate changes. The GLASS LWDN is produced using the backup algorithm (3) for the Tibetan Plateau.

As shown in Fig. 19, LWUP is in satisfactory agreement with the measured LWUP in the daytime and is underestimated at the nighttime, with biases and RMSEs of 2.55 and 20.46 W/m^2 in the daytime and –16.06 and 24.99 W/m^2 at the nighttime. The overall bias and RMSE for LWUP is –9.43 and 23.47 W/m^2, as specified in Table I in Section III-A. This accuracy is slightly higher than that of Jiao *et al*. [7]. Their hybrid method for LWUP estimation has a bias of 10.82 W/m^2 and an RMSE of 26.99 W/m^2 when validated over the Tibetan Plateau. In addition, the accuracy of LWUP in this study is higher than those of GEWEX-SRB, ISCCP-FD, CERES-FSW, and LWUP that were estimated via Wang's method [21]. According to the validation results of Gui *et al*. [10], the bias are 9.8, 21.0, –12.3 and –12.7 W/m^2, and the RMSEs are 30.4, 26.6, 29.8, and 16.2 W/m^2 for GEWEX-SRB, ISCCP-FD, CERES-FSW, and LWUP, respectively, that were estimated via Wang's method [21] over the Tibetan Plateau.

The LW radiation is overestimated in the daytime and significantly underestimated during the nighttime. Since the TIPEX-III sites are almost in the valley, the main causes may be the complex terrain effect, which is not considered in our retrieval algorithms. LWUP and LWDN radiation retrieval in the valley is influenced by four main factors: obstruction in the solar direction, contribution of the LW radiation from the surrounding terrain, nearby terrains, and the invisibility of some pixels to the sensor due to terrain undulation [80]. During the daytime, the effective radiating temperatures of the radiating sky and the surrounding terrain when the slopes are strongly heated by the sunlight are warmer than the cold atmosphere of the surface measurements in the valley under clear-sky conditions, which leads to the satellite-derived LWDN being larger than the surface measurements [81]. The discrepancy between the cold radiating sky and the warmer terrain can result in a difference of approximately 50 W/m^2 in LWDN between the valley floor and ridge, which causes large biases in the retrieved surface LW radiation [82]–[84]. During the nighttime, LWUP is underestimated because the surface thermal radiation of the nearby terrain is blocked by surrounding terrain, and a satellite sensor such as MODIS can only receive surface radiance from a single direction [85]. For a deep valley, LWDN has two sources: the LW radiation from the atmosphere and the contribution of LW radiation from the surrounding terrain. Since the pyrgeometers measure both of them, LWDN is underestimated. For LWNR, the accuracy depends on the accuracies of LWUP and LWDN, the underestimation of LWNR may be due more to the surrounding terrain emission thermal radiation than to blocking by nearby terrain.

V. Conclusion

In view of the significant role of satellite-derived surface LW radiation products in the study of climate change and the need by related research communities for long-time-series high-quality surface LW radiation products, we developed algorithms for the retrieval of high-spatial-resolution surface LW radiation products and we produced a long-time-series all-sky instantaneous GLASS LW radiation product. To determine the accuracy and uncertainty of the GLASS LW radiation product, we comprehensively evaluated the GLASS LW radiation product using LW radiation measurements that were collected from sites in six independent networks (AmeriFlux, AsiaFlux, BSRN, CEOP, HiWATER-MUSOEXE, and TIPEX-III). According to the evaluation results, the biases are –4.33, –3.77, and 0.70 W/m^2 and the RMSEs are 18.15, 26.94, and 26.70 W/m^2 for clear-sky LWUP, LWDN, and LWNR, respectively. Comparing to previous evaluation studies, our LW radiation product outperforms GEWEX-SRB, ISCCP-FD, and CERES-FSW in terms of overall accuracy, with the exception of LWDN, for which the RMSE of our product was larger.

The performances of the GLASS LW radiation product for day and night, Terra and Aqua, land and ocean, and each network are also evaluated. The evaluation results are consistent with the overall accuracy. In addition, the effects of the land cover type, the climatic type, and the surface elevations on the performance of the GLASS LW radiation product are analyzed. The GLASS LW radiation product performs well in climate-change-sensitive areas. For example, the accuracy of GLASS LWDN is comparable to that of GEWES SRB LWDN. The comparison results demonstrate that the GLASS LWUP product outperforms the CERES SSF instantaneous LW product in semiarid regions. The accuracy of LWUP is higher than those of previous studies and products for the Tibetan Plateau.

According to the evaluation results, the overall accuracy of the clear-sky GLASS LW radiation product can satisfy the requirement of 20 W/m^2 and degrades under identified conditions. We will continue to improve the retrieval algorithms and update the products.

Appendix

TABLE VII
DETAILED INFORMATION OF EACH SITE

Short Name	Full Name	Latitude (deg)	Longitude (deg)	Elevation (m)	Land Cover	Climatic Type	Temporal Resolution	Time Period	Instrument
CLM[f]	Chi-Lan Mountain Research Site	24.58	121.40	1600	Forests	Cfb	30	2007-2009	Eppley, PIR
KBU[a]	Kherlenbayan Ulaan	47.21	108.74	1235	Forests	Bsk	30	2006-2008	Kipp&Zonen CNR-1
MBF[a]	Moshiri Birch Forest	44.38	142.32	585	Forests	Dfb	30	2003-2005	Kipp&Zonen CNR-1
MMF[a]	Moshiri Mixed Forest	44.32	142.26	340	Forests	Dfb	30	2003-2005	Kipp&Zonen CNR-1
PDF[a]	Palangkaraya drained forest	-2.35	114.04	30	Forests	Af	60	2003-2005	Kipp&Zonen CNR-1
PSO[a]	Pasoh Forest Reserve	2.97	102.31	75-150	Forests	Af	30	2007-2009	Kipp&Zonen CNR-1
SMF[a]	Seto Mixed Forest	35.26	137.08	205	Forests	Cfa	30	2005-2007	Kipp&Zonen CNR-1
TKY[a]	Takayama deciduous broadleaf forest	36.15	137.42	1420	Forests	Dfb	30	2005-2007	-
YLF[a]	Siberia Yakutsk Larch Forest	62.26	129.17	220	Forests	Dfd	30	2005-2007	EKO MS 201F
YPF[a]	Yakutsk Pine Forest	62.24	129.65	220	Forests	Dfd	30	2005-2007	EKOMS-201F
US-Aud[b]	Audubon Research Ranch	31.59	-110.51	1469	Grasslands	Bsk	30	2004-2006	Kipp&Zonen CNR-1
US-Bo1[b]	Bondville	40.01	-88.29	219	Croplands	Dfa	30	2004-2006	Kipp&Zonen CNR-1
US-Bo2[b]	Bondville (companion site)	40.01	-88.29	219	Croplands	Dfa	30	2004-2006	Kipp&Zonen CNR-1
US-Dk1[b]	Duke Forest-open field	35.97	-79.09	168	Grasslands	Cfa	30	2004-2006	Kipp&Zonen CNR-1 lite
US-Dk2[b]	Duke Forest-hardwoods	35.97	-79.10	168	Forests	Cfa	30	2004-2006	Kipp&Zonen CNR-1 lite
US-Dk3[b]	Duke Forest loblolly pine	35.98	-79.09	163	Forests	Cfa	30	2004-2006	Kipp&Zonen CNR-1 lite
US-Fmf[b]	Flagstaff-Managed Forest	35.14	-111.73	2160	Forests	Csb	30	2008-2010	Kipp&Zonen CNR-1
US-FPe[b]	Fort Peck	48.31	-105.10	634	Grasslands	Bsk	30	2004-2006	Kipp&Zonen CNR-1
US-Fuf[b]	Flagstaff-Unmanaged Forest	35.09	-111.76	2180	Forests	Csb	30	2008-2010	Kipp&Zonen CNR-1
US-Fwf[b]	Flagstaff-Wildfire	35.45	-111.77	2270	Grasslands	Csb	30	2008-2010	Kipp&Zonen CNR-1
US-GLE[b]	GLEES	41.37	-106.24	3197	Forests	Dfc	30	2012-2014	Eppley, PIR
US-Ho1[b]	Howland Forest (main tower)	45.20	-68.74	60	Forests	Dfb	30	2012-2014	Kipp&Zonen CNR-1
US-Ho3[b]	Howland Forest (harvest site)	45.21	-68.73	61	Forests	Dfb	30	2007-2009	Kipp&Zonen CNR-1
US-Ivo[b]	Ivotuk	68.49	-155.75	568	Wetlands	ET	30	2004-2006	Kipp&Zonen CNR-1
US-KFS[b]	Kansas Field Station	39.06	-95.19	310	Grasslands	Cfa	30	2008-2010	-
US-MRf[b]	Mary's River (Fir) site	44.65	-123.55	263	Forests	Csb	30	2008-2010	-
US-Ne1[b]	Mead-irrigated continuous maize site	41.17	-96.48	361	Croplands	Dfa	60	2004-2006	Kipp&Zonen CNR-1
US-Ne2[b]	Mead-irrigated maize-soybean rotation site	41.16	-96.47	362	Croplands	Dfa	60	2004-2006	Kipp&Zonen CNR-1
US-Ne3	Mead-rainfed maize-soybean rotation site	41.18	-96.44	363	Croplands	Dfa	60	2004-2006	Kipp&Zonen CNR-1
US-NR1	Niwot Ridge Forest	40.03	-105.55	3050	Forests	Dfc	30	2012-2014	Kipp&Zonen CNR-1
US-Ses	Sevilleta shrubland	34.33	-106.74	1604	Shrublands	Bsk	30	2012-2014	Kipp&Zonen CNR-1
US-SFP	Sioux Falls Portable	43.24	-96.90	386	Grasslands	Dfa	30	2007-2009	
US-Slt	Silas Little-New Jersey	39.91	-74.60	30	Forests	Dfa	30	2012-2014	Kipp&Zonen CNR-1 lite
US-SRC[b]	Santa Rita Creosote	31.91	-110.84	991	Shrublands	Bwh	30	2009-2011	-
US-SRM[b]	Santa Rita Mesquite	31.82	-110.87	1120	Savannas	Bsk	30	2012-2014	-
US-UMB[b]	Univ. of Mich. Biological Station	45.56	-84.71	234	Forests	Dfb	30	2012-2014	Kipp&Zonen CNR-1
US-UMd[b]	UMBS Disturbance	45.56	-84.70	239	Forests	Dfb	30	2012-2014	Kipp&Zonen CNR-1
US-Var[b]	Vaira Ranch-Ione	38.41	-120.95	129	Grasslands	Csa	30	2012-2014	Kipp&Zonen CNR-1
US-Vcp[b]	Valles Caldera Ponderosa Pine	35.86	-106.60	2500	Forests	Dfb	30	2012-2014	
US-Whs[b]	Walnut Gulch Lucky Hills Shrub	31.74	-110.05	1370	Shrublands	Bsk	30	2012-2014	
ALE[c]	Alert	82.49	-62.42	127	Tundra	ET	1	2011-2013	Eppley, PIR
BAR[c]	Barrow	71.32	-156.61	8	Tundra	ET	1	2014-2016	Eppley, PIR
BER[c]	Bermuda	32.27	-64.67	8	Water	/	1	2008-2010	Eppley, PIR
BRB[c]	Brasilia	-15.60	-47.71	1023	Urban and Built-up Lands	Aw	1	2013-2015	Eppley, PIR
CAB[c]	Cabauw	51.97	4.93	0	Grasslands	Cfb	1	2014-2016	Kipp&Zonen CG-4
CAM[c]	Camborne	50.22	-5.32	88	Grasslands	Cfb	1	2014-2016	Eppley, PIR
CAR[c]	Carpentras	44.08	5.06	100	Croplands	Csa	1	2014-2016	Eppley, PIR
CLH[c]	Chesapeake Light	36.91	-75.71	37	Water	/	1	2010-2012	Eppley, PIR
CNR[c]	Cener	42.82	-1.60	471	Urban and Built-up Lands	Cfb	1	2014-2016	Kipp&Zonen CG-4
COC[c]	Cocos Island	-12.19	96.84	6	Grasslands	Af	1	2015-2017	Eppley, PIR
DOM[c]	Concordia Station, Dome C	-75.10	123.38	3233	Ice	ET	1	2014-2016	Kipp&Zonen CG-4
DWN[c]	Darwin Met Office	-12.42	130.89	32	Grasslands	Aw	1	2015-2017	Eppley, PIR
FLO[c]	Florianopolis	-27.60	-48.52	11	Urban and Built-up Lands	Cfa	1	2014-2016	Eppley, PIR
FUA[c]	Fukuoka	33.58	130.38	3	Urban and Built-up Lands	Cfa	1	2015-2017	Kipp&Zonen CG-4
GOB[c]	Gobabeb	-23.56	15.04	407	Barren Land	Bwh	1	2015-2017	Eppley, PIR
GVN[c]	Georgvon Neumayer	-70.65	-8.25	42	Ice	ET	1	2015-2017	Eppley, PIR
ISH[c]	Ishigakijima	24.34	124.16	5.7	Urban and Built-up Lands	Af	1	2015-2017	Kipp&Zonen CG-4
IZA[c]	Izaña	28.31	-16.50	2372.9	Urban and Built-up Lands	Csb	1	2015-2017	Kipp&Zonen CG-4
KWA[c]	Kwajalein	8.72	167.73	10	Water	Af	1	2014-2016	Eppley, PIR
LIN[c]	Lindenberg	52.21	14.12	125	Croplands	Dfb	1	2014-2016	Eppley, PIR
LER[c]	Lerwick	60.14	-1.18	80	Grasslands	Cfc	1	2014-2016	Eppley, PIR
MNM[c]	Minamitorishima	24.29	153.98	7.1	Water	/	1	2015-2017	Kipp&Zonen CG-4
PAL[c]	Palaiseau, SIRTA Observatory	48.71	2.21	156	Urban and Built-up	Cfb	1	2014-2016	Kipp&Zonen CG-4

[a]AsiaFlux Sites; [b]AmeriFlux Sites; [c]CEOP Sites; [d]BSRN Sites; [e]TIPEX-III Sites; [f]HIWTER-MUSOEXE Sites; [g]Köppen climate classification(http://www.gloh2o.org/koppen/).

ACKNOWLEDGMENT

The AmeriFlux data were downloaded from https://ameriflux.lbl.gov/data/download-data/, the AsiaFlux data were downloaded from https://db.cger.nies.go.jp/asiafluxdb/, the BSRN data ere downloaded from http://www.bsrn.awi.de/, the CEOP data were downloaded from http://aan.suiri.tsukuba.ac.jp, the HiWATER-MUSOEXE data were downloaded from http://www.heihedata.org/, and the TIPEX-III data were downloaded from http://123.56.215.19/tipex/expeditionData/id/3.html. The MODIS data were obtained from http://reverb.echo.nasa.gov/reverb/.

REFERENCES

[1] J. Cheng, W. Wang, S. Liang, F. Yang, and S. Zhou, "Surface longwave radiation budget," in *Advanced Remote Sensing*, 2nd ed., S. Liang and J. Wang, Eds. New York, NY, USA: Academic, 2020, pp. 297–347, ch. 8.

[2] S. Liang, D. Wang, T. He, and Y. Yu, "Remote sensing of earth's energy budget: Synthesis and review," *Int. J. Digit. Earth*, no. 9, pp. 1–44, 2019.

[3] W. Wang and S. Liang, "Estimation of high-spatial resolution clear-sky longwave downward and net radiation over land surfaces from MODIS data," *Remote Sens. Environ.*, vol. 113, no. 4, pp. 745–754, 2009.

[4] E. A. Nussbaumer and R. T. Pinker, "Estimating surface longwave radiative fluxes from satellites utilizing artificial neural networks," *J. Geophysical Res.*, vol. 117, no. D07209, 2012, doi: 10.1029/2011JD017141.

[5] M. Wild, A. Ohmura, H. Gilgen, J. J. Morcrette, and A. Slingo, "Evaluation of downward longwave radiation in general circulation models," *J. Climate*, vol. 15, no. 15, pp. 3227–3239, 2001.

[6] Y. Zhou and R. D. Cess, "Algorithm development strategies for retrieving the downwelling longwave flux at the earth's surface," *J. Geophysical Res. Atmos.*, vol. 106, no. D12, pp. 12477–12488, 2001.

[7] Z. Jiao, G. Yan, J. Zhao, T. Wang, and L. Chen, "Estimation of surface upward longwave radiation from MODIS and VIIRS clear-sky data in the Tibetan Plateau," *Remote Sens. Environ.*, vol. 162, pp. 221–237, 2015.

[8] T. Wang *et al.*, "Cloudy-sky land surface longwave downward radiation (LWDR) estimation by integrating MODIS and AIRS/AMSU measurements," *Remote Sens. Environ.*, vol. 205, pp. 100–111, 2018.

[9] S. Zhou and J. Cheng, "Estimation of high spatial-resolution clear-sky land surface-upwelling longwave radiation from VIIRS/S-NPP data," *Remote Sens.*, vol. 10, no. 2, Feb. 2018, doi: 10.1029/2011JD017141.

[10] S. Gui, S. Liang, and L. Li, "Evaluation of satellite-estimated surface longwave radiation using ground-based observations," *J. Geophysical Res.*, vol. 115, no. D18, 2010, doi: 10.1029/2009JD013635.

[11] Z. Wan, "New refinements and validation of MODIS land-surface temperature/emissivity products," *Remote Sens. Environ.*, vol. 112, no. 1, pp. 59–74, 2008.

[12] Y. Yu, Y. Liu, P. Yu, Y. Liu, and P. Yu, "5.12—Land surface temperature product development for JPSS and GOES-R missions," *Comprehensive Remote Sensing*, S. Liang, Ed. Oxford, U.K.: Elsevier, 2018, pp. 284–303.

[13] F.-M. Göttsche, F.-S. Olesen, F. I. Trigo, A. Bork-Unkelbach, and A. M. Martin, "Long term validation of land surface temperature retrieved from MSG/SEVIRI with continuous in-situ measurements in Africa," *Remote Sens.*, vol. 8, no. 5, 2016.

[14] J. Cheng and S. Liang, "Estimating the broadband longwave emissivity of global bare soil from the MODIS shortwave albedo product," *J. Geophysical Res.-Atmos.*, vol. 119, no. 2, pp. 614–634, 2014.

[15] J. Cheng, S. Liang, W. Verhoef, S. Shi, and Q. Liu, "Estimating the hemispherical broadband longwave emissivity of global vegetated surfaces using a radiative transfer model," *IEEE Trans. Geosci. Remote Sens.*, vol. 54, no. 2, pp. 905–917, Feb. 2016.

[16] S. Liang *et al.*, "A long-term global land surface satellite (GLASS) data-set for environmental studies," *Int. J. Digit. Earth*, vol. 6, no. sup1, pp. 5–33, 2013.

[17] J. Cheng, S. Liang, Y. Yao, and X. Zhang, "Estimating the optimal broadband emissivity spectral range for calculating surface longwave net radiation," *IEEE Geosci. Remote Sens. Lett.*, vol. 10, no. 2, pp. 401–405, Mar. 2013.

[18] W. Wang, S. Liang, and T. Meyers, "Validating MODIS land surface temperature products using long-term nighttime ground measurements," *Remote Sens. Environ.*, vol. 112, no. 3, pp. 623–635, 2008.

[19] K. Wang and S. Liang, "Evaluation of ASTER and MODIS land surface temperature and emissivity products using long-term surface longwave radiation observations at SURFRAD sites," *Remote Sens. Environ.*, vol. 113, no. 7, pp. 1556–1565, 2009.

[20] S. Liang, K. Wang, X. Zhang, and M. Wild, "Review of estimation of land surface radiation and energy budgets from ground measurements, remote sensing and model simulation," *IEEE J. Sel. Topics Appl. Earth Observ. Remote Sens.*, vol. 3, no. 3, pp. 225–240, Sep. 2010.

[21] W. Wang, S. Liang, and J. A. Augustine, "Estimating high spatial resolution clear-sky land surface upwelling longwave radiation from MODIS data," *IEEE Trans. Geosci. Remote Sens.*, vol. 47, no. 5, pp. 1559–1570, May 2009.

[22] B. Tang and Z.-L. Li, "Estimating of instantaneous net surface longwave radiation from MODIS cloud-free data," *Remote Sens. Environ.*, vol. 112, pp. 3482–3492, 2008.

[23] T. Wang, G. Yan, and L. Chen, "Consistent retrieval methods to estimate land surface shortwave and longwave radiative flux components under clear-sky conditions," *Remote Sens. Environ.*, vol. 124, no. 9, pp. 61–71, 2012.

[24] S. S. Yu, X. Z. Xin, and Q. H. Liu, "Estimation of clear-sky longwave downward radiation from HJ-1B thermal data," *Sci. China Earth Sci.*, vol. 56, no. 5, pp. 829–842, 2013.

[25] D. Brunt, "Notes on radiation in the atmosphere. I," *Quart. J. Roy. Meteorological Soc.*, vol. 58, no. 247, pp. 389–420, 1932.

[26] T. M. Crawford and C. E. Duchon, "An improved parameterization for estimating effective atmospheric emissivity for use in calculating daytime downwelling longwave radiation," *J. Appl. Meteorol.*, vol. 38, no. 4, pp. 474–480, 1999.

[27] F. Carmona, R. Rivas, and V. Caselles, "Estimation of daytime downward longwave radiation under clear and cloudy skies conditions over a subhumid region," *Theor. Appl. Climatol.*, vol. 115, no. 1-2, pp. 281–295, 2014.

[28] H. F. Duarte, N. L. Dias, and S. R. Maggiotto, "Assessing daytime downward longwave radiation estimates for clear and cloudy skies in southern Brazil," *Agricultural Forest Meteorol.*, vol. 139, no. 3-4, pp. 171–181, 2006.

[29] T. Konzelmann, R. S. van de Wal, W. Greuell, R. Bintanja, E. A. Henneken, and A. Abe-Ouchi, "Parameterization of global and longwave incoming radiation for the Greenland Ice Sheet," *Global Planet. Change*, vol. 9, no. 1-2, pp. 143–164, 1994.

[30] J.-P. Lhomme, J.-J. Vacher, and A. Rocheteau, "Estimating downward long-wave radiation on the Andean Altiplano," *Agricultural Forest Meteorol.*, vol. 145, no. 3-4, pp. 139–148, 2007.

[31] A. Prata, "A new long-wave formula for estimating downward clear-sky radiation at the surface," *Quart. J. Roy. Meteorological Soc.*, vol. 122, no. 533, pp. 1127–1151, 1996.

[32] J. Cheng, F. Yang, and Y. Guo, "A comparative study of bulk parameterization schemes for estimating cloudy-sky surface downward longwave radiation," *Remote Sens.*, vol. 11, no. 5, Mar 1, 2019, doi: 10.3390/rs11050528.

[33] Y. Guo, J. Cheng, and S. Liang, "Comprehensive assessment of parameterization methods for estimating clear-sky surface downward longwave radiation," *Theor. Appl. Climatol.*, vol. 135, no. 3-4, pp. 1045–1058, Feb. 2019.

[34] Y. Zhou, D. P. Kratz, A. C. Wilber, S. K. Gupta, and R. D. Cess, "An improved algorithm for retrieving surface downwelling longwave radiation from satellite measurements," *J. Geophysical Res.*, vol. 112, no. D15, 2007, doi: 10.1029/2006JD008159.

[35] B. A. Forman and S. A. Margulis, "High-resolution satellite-based cloud-coupled estimates of total downwelling surface radiation for hydrologic modelling applications," *Hydrol. Earth Syst. Sci.*, vol. 6, no. 2, pp. 969–986, 2009.

[36] S. K. Gupta, W. L. Darnell, and A. C. Wilber, "A parameterization for longwave surface radiation from satellite data: Recent improvements," *J. Appl. Meteorol.*, vol. 31, no. 12, pp. 1361–1367, 1992.

[37] W. Wang and S. Liang, "A method for estimating clear-sky instantaneous land-surface longwave radiation with GOES sounder and GORE-R ABI data," *IEEE Geosci. Remote Sens. Lett.*, vol. 7, no. 4, pp. 708–712, 2010.

[38] X. M. Zhou, B. H. Tang, H. Wu, and Z. L. Li, "Estimating net surface longwave radiation from net surface shortwave radiation for cloudy skies," *Int. J. Remote Sens.*, vol. 34, no. 22, pp. 8104–8117, 2013.

[39] Y. Guo and J. Cheng, "Feasibility of estimating cloudy-sky surface longwave net radiation using satellite-derived surface shortwave net radiation," *Remote Sens.*, vol. 10, no. 4, Apr. 2018, doi: 10.3390/rs10040596.

[40] Y. C. Zhang, W. Rossow, and A. Lacis, "Calculation of surface and top of atmosphere radiative fluxes from physical quantities based on ISCCP data sets: 1. Method and sensitivity to input data uncertainties," *J. Geophysical Res., Atmos.*, vol. 100, no. D1, pp. 1149–1165, 1995.

[41] Y. Zhang, W. B. Rossow, A. A. Lacis, V. Oinas, and M. I. Mishchenko, "Calculation of radiative fluxes from the surface to top of atmosphere based on ISCCP and other global data sets: Refinements of the radiative transfer model and the input data," *J. Geophysical Res., Atmos.*, vol. 109, no. D19, 2004, doi: 10.1029/2003JD004457.

[42] Y. Zhang, W. B. Rossow, and P. W. Stackhouse Jr., "Comparison of different global information sources used in surface radiative flux calculation: Radiative properties of the surface," *J. Geophysical Res., Atmos.*, vol. 112, no. D1, 2007, doi: 10.1029/2003JD004457.

[43] Q. Fu and K. N. Liou, "Parameterization of the radiative properties of cirrus clouds," *J. Atmospheric Sci.*, vol. 50, no. 13, pp. 2008–2025, 1993.

[44] R. T. Pinker *et al.*, "Surface radiation budgets in support of the GEWEX continental-scale international project (GCIP) and the GEWEX americas prediction project (GAPP), including the north american land data assimilation system (NLDAS) project," *J. Geophysical Res., Atmos.*, vol. 108, no. D22, 2003.

[45] B. A. Wielicki, B. R. Barkstrom, E. F. Harrison, R. B. Lee, III, G. L. Smith, and J. E. Cooper, "Clouds and the earth's radiant energy system (CERES): An earth observing system experiment," *Bull. Amer. Meteorological Soc.*, vol. 77, no. 5, pp. 853–868, 1996.

[46] A. K. Inamdar and V. Ramanathan, "On monitoring the atmospheric greenhouse effect from space," *Tellus Series B Chem. Physical Meteorol.*, vol. 49, no. 2, pp. 216–230, 1997.

[47] R. D. Cess *et al.*, "Absorption of solar radiation by clouds: Observations versus models," *Science*, vol. 267, no. 5197, pp. 496–499, 1995.

[48] T. Zhang, P. W. Stackhouse, S. K. Gupta, S. J. Cox, and J. C. Mikovitz, "The validation of the GEWEX SRB surface longwave flux data products using BSRN measurements," *J. Quantitative Spectrosc. Radiative Transfer*, vol. 150, pp. 134–147, 2015.

[49] H. Yan, J. Huang, P. Minnis, T. Wang, and J. Bi, "Comparison of CERES surface radiation fluxes with surface observations over Loess Plateau," *Remote Sens. Environ.*, vol. 115, no. 6, pp. 1489–1500, 2011.

[50] D. P. Kratz, S. K. Gupta, A. C. Wilber, and V. E. Sothcott, "Validation of the CERES edition 2B surface-only flux algorithms," *J. Appl. Meteorol. Climatol.*, vol. 49, no. 1, pp. 164–180, 2010.

[51] V. Masson, J.-L. Chameraux, F. Chauvin, C. meriguet, and R. Lacaze, "A global database of land surface parameters at 1-km resolution in meteorological and climate models," *J. Climate*, vol. 16, no. 9, pp. 1261–1282, 2003.

[52] O. B. Christensen and J. H. Christensen, "Very high-resolution regional climate simulations over scandinavia-present climate," *J. Climate*, vol. 11, no. 12, pp. 3204–3229, 1998.

[53] S. Liang *et al.*, "Validating MODIS land surface reflectance and albedo products: Methods and preliminary results," *Remote Sens. Environ.*, vol. 83, no. 1-2, pp. 149–162, 2002.

[54] J. Cheng and S. Liang, "Global estimates for high-spatial-resolution clear-sky land surface upwelling longwave radiation from MODIS data," *IEEE Trans. Geosci. Remote Sens.*, vol. 54, no. 7, pp. 4115–4129, Jul. 2016.

[55] J. Cheng, S. Liang, W. Wang, and Y. Guo, "An efficient hybrid method for estimating clear-sky surface downward longwave radiation from MODIS data," *J. Geophysical Res.-Atmospheres*, vol. 122, no. 5, pp. 2616–2630, Mar. 16, 2017.

[56] Z. Wan and J. Dozier, "A generalized split-window algorithm for retrieving land-surface temperature form space," *IEEE Trans. Geosci. Remote Sens.*, vol. 34, no. 4, pp. 892–905, 1996.

[57] B. A. Forman and S. A. Margulis, "Estimates of total downwelling surface radiation using a high-resolution GOES-based cloud product along with MODIS and AIRS products," American Geophysical Union, 2007.

[58] G. Bisht and R. L. Bras, "Estimation of net radiation from the MODIS data under all sky conditions: Southern Great Plains case study," *Remote Sens. Environ.*, vol. 114, no. 7, pp. 1522–1534, Jul. 15, 2010.

[59] W. Zhou *et al.*, "New methods for deriving clear-sky surface longwave downward radiation based on remotely sensed data and ground measurements," *Earth Space Sci.*, vol. 6, no. 11, pp. 2017–2086, 2019.

[60] D. Baldocchi *et al.*, "FLUXNET: A new tool to study the temporal and spatial variability of ecosystem-scale carbon dioxide, water vapor, and energy flux densities," *Bull. Amer. Meteorological Soc.*, vol. 82, no. 11, pp. 2415–2434, 2001.

[61] S. Liu *et al.*, "Upscaling evapotranspiration measurements from multi-site to the satellite pixel scale over heterogeneous land surfaces," *Agricultural Forest Meteorol.*, vol. 230, pp. 97–113, 2016.

[62] Z. Xu *et al.*, "Intercomparison of surface energy flux measurement systems used during the HiWATER-MUSOEXE," *J. Geophysical Res. Atmos.*, vol. 118, no. 23, pp. 13–13, 2013.

[63] P. Zhao *et al.*, "The third atmospheric scientific experiment for understanding the earth–atmosphere coupled system over the Tibetan Plateau and its effects," *Bull. Amer. Meteorological Soc.*, vol. 99, no. 4, pp. 757–776, 2018.

[64] W. L. Smith and H. M. Wolfe, "Geostationary satellite sounder (VAS) observations of longwave radiation flux," in *The Satellite Systems to Measure Radiation Budget Parameters and Climate Signal*, Igls, Austria, International Radiation Commission, 1983.

[65] S. Liang, J. Stroeve, and J. E. Box, "Mapping daily snow/ice shortwave broadband albedo from moderate resolution imaging spectroradiometer (MODIS): The improved direct retrieval algorithm and validation with Greenland in situ measurement," *J. Geophysical Res.*, vol. 110, no. 110, pp. 1223–1242, 2005.

[66] M. K. Yau, and R. R. Rogers, *A Short Course in Cloud Physics*. Amsterdam, The Netherlands: Elsevier, 1996.

[67] J. Cheng and S. Liang, "Effects of thermal-infrared emissivity directionality on surface broadband emissivity and longwave net radiation estimation," *IEEE Geosci. Remote Sens. Lett.*, vol. 11, no. 2, pp. 499–503, Feb. 2014.

[68] G. Bisht and R. L. Bras, "Estimation of net radiation from the moderate resolution imaging spectroradiometer over the continetal united states," *IEEE Trans. Geosci. Remote Sens.*, vol. 49, no. 6, pp. 2448–2462, Jun. 2011.

[69] P. Minnis, D. R. Doelling, L. Nguyen, W. F. Miller, and V. Chakrapani, "Assessment of the visible channel calibrations of the VIRS on TRMM and MODIS on aqua and terra," *J. Atmospheric Oceanic Technol.*, vol. 25, no. 3, pp. 385–400, 2008.

[70] J. Cheng and P. W. Kustas, "Using very high resolution thermal infrared imagery for more accurate determination of the impact of land cover differences on evapotranspiration in an irrigated agricultural area," *Remote Sens.*, vol. 11, no. 6, 2019, doi: 10.3390/rs11060613.

[71] A. Christen and R. Vogt, "Energy and radiation balance of a central European city," *Int. J. Climatol., A J. Roy. Meteorological Soc.*, vol. 24, no. 11, pp. 1395–1421, 2004.

[72] A. J. Arnfield, "An approach to the estimation of the surface radiative properties and radiation budgets of cities," *Physical Geography*, vol. 3, no. 2, pp. 97–122, 1982.

[73] B. Offerle, C. S. B. Grimmond, K. Fortuniak, and W. Pawlak, "Intraurban differences of surface energy fluxes in a central European city," *J. Appl. Meteorol. Climatol.*, vol. 45, no. 1, pp. 125–136, 2006.

[74] C. M. Naud, J. R. Miller, and C. Landry, "Using satellites to investigate the sensitivity of longwave downward radiation to water vapor at high elevations," *J. Geophysical Res., Atmos.*, vol. 117, no. D5, 2012, Art. no. D05101.

[75] W. Köppen and R. Geiger, *Handbuch Der Klimatologie*. Berlin, Germany: Gebrüder Borntraeger, 1930.

[76] J. C. King and W. M. Connolley, "Validation of the surface energy balance over the antarctic ice sheets in the U.K. Meteorological office unified climate model," *J. Climate*, vol. 10, no. 10, pp. 1273–1287, 1997.

[77] Q. Fu, C. M. Johanson, J. M. Wallace, and T. Reichler, "Enhanced mid-latitude tropospheric warming in satellite measurements," *Science*, vol. 312, no. 5777, pp. 1179–1179, 2006.

[78] J. D. Hansom and J. Gordon, *Antarctic Environments and Resources: A Geographical Perspective*. Evanston, IL, USA: Routledge, 2014.

[79] S. K. Gupta, D. P. Kratz, P. W. Stackhouse, A. C. Wilber, T. Zhang, and V. E. Sothcott, "Improvement of surface longwave flux algorithms used in CERES processing," *J. Appl. Meteorol. Climatol.*, vol. 49, no. 7, pp. 1579–1589, 2010.

[80] G. Yan, T. Wang, Z. Jiao, X. Mu, J. Zhao, and L. Chen, "Topographic radiation modeling and spatial scaling of clear-sky land surface longwave radiation over rugged terrain," *Remote Sens. Environ.*, vol. 172, pp. 15–27, Jan. 2016.

[81] N. Matzinger, M. Andretta, E. V. Gorsel, R. Vogt, A. Ohmura, and M. Rotach, "Surface radiation budget in an Alpine valley," *Quart. J. Roy. Meteorological Soc., A J. Atmospheric Sci., Appl. Meteorol. Physical Oceanogr.*, vol. 129, no. 588, pp. 877–895, 2003.

[82] N. Matzinger, M. Andretta, E. V. Gorsel, R. Vogt, and M. W. Rotach, "Surface radiation budget in an Alpine valley," *Quart. J. Roy. Meteorological Soc.*, vol. 129, no. 588, pp. 877–895, 2010.

[83] J. Manners, S. B. Vosper, and N. Roberts, "Radiative transfer over resolved topographic features for high-resolution weather prediction," *Quart. J. Roy. Meteorological Soc.*, vol. 138, no. 664, pp. 720–733, 2012.
[84] A. J. Oliphant, R. A. Spronken-Smith, A. P. Sturman, and I. F. Owens, "Spatial variability of surface radiation fluxes in mountainous terrain," *J. Appl. Meteorol.*, vol. 42, no. 42, pp. 113–128, 2003.
[85] G. Yan, Z.-H. Jiao, T. Wang, and X. Mu, "Modeling surface longwave radiation over high-relief terrain," *Remote Sens. Environ.*, vol. 237, 2020, Art. no. 111556.

Qi Zeng is currently working toward the Ph.D. degree in cartography and geographic information system with Beijing Normal University, Beijing, China.

Her research interests include the estimate of the component of surface radiation budget, validation of surface longwave radiation product, and time-scale extend of surface longwave radiation.

Jie Cheng (Senior Member, IEEE) received the Ph.D. degree in cartography and remote sensing from the Institute of Remote Sensing Applications, Chinese Academy of Sciences, Beijing, China, in 2008.

He was a Postdoctoral Fellow with the State Key Laboratory of Remote Sensing Science, Beijing Normal University, Beijing, China, from 2008 to 2010, an Assistant Research Scientist with the University of Maryland, College Park, MD, USA, from 2009 to 2010, and a Visiting Scientist with the Hydrology and Remote Sensing Laboratory, United States Department of Agriculture-Agricultural Research Service, Beltsville, MD, USA, from 2017 to 2018. He is currently an Associate Professor with the State Key Laboratory of Remote Sensing Science, Faculty of Geographical Science, Beijing Normal University. He authored and coauthored more than 60 SCI indexed peer-reviewed papers, seven book chapters, and two special issues of *Remote Sensing*. His main research interests include estimation of land surface variables from satellite observations, radiative transfer modeling, and studies on surface energy balance.

Lixin Dong received the B.S. degree in applied meteorology from Nanjing Meteorological College, Nanjing, China, in 1995, and the Ph.D. degree in geographic information and map cartography from the Chinese Academy of Sciences, Beijing, China, in 2008.

He is currently an Associate Professor with the National Satellite and Meteorological Center, China Meteorological Administration, Beijing, China. From July to August 2017, he was a Visiting Scholar with the Hydrology and Remote Sensing Laboratory of Agricultural Research Services Department, United States Department of Agriculture. His research interests include the LiDAR data processing algorithm and application, the land surface temperature and soil moisture algorithms of FengYun satellite imagery, and the atmospheric radiative transfer model.